Assessing Human Appropriation of Net Primary Production in Various Vegetation Types Based on the Spatio-Temporal Fusion Model in Xiong'an New Area During 2000-2018

Jia Tang
Fuzhou University
Qing Zhang
Institute of Remote Sensing and Digital Earth Chinese Academy of Sciences
Jingyu Zeng
Fuzhou University
Rongrong Zhang
Fuzhou University
Xingrong Li
Institute of Remote Sensing and Digital Earth Chinese Academy of Sciences
Yanqin Tian
Institute of Remote Sensing and Digital Earth Chinese Academy of Sciences
Qianfeng Wang (wangqianfeng@fzu.edu.cn)
Fuzhou University

Research

Keywords: Spatio-temporal fusion, Mann–Kendall trend analysis, Human appropriation of net primary production, Dynamic, Driven factors

Posted Date: November 6th, 2020

DOI: https://doi.org/10.21203/rs.3.rs-59359/v2

Assessing human appropriation of net primary production in various vegetation types based on the spatio-temporal fusion model in Xiong'an New Area during 2000-2018

Jia Tang [1]. Qing Zhang [2]. Jingyu Zeng [1]. Rongrong Zhang [1]. Xingrong Li[2] . Yanqin Tian[2]. Qianfeng Wang[1,3,*]

Abstract

Background: Humans have induced great changes in terrestrial ecosystems. The human appropriation of net primary production (HANPP) quantifying the intensity of anthropogenic extraction from ecosystem has been widely used to evaluate ecological sustainable development. However, the coarse-resolution of calculating data for the HANPP leads to biased results in a small scale. Furthermore, the spatio-temporal patterns and dynamics of the HANPP in a human-dominated heterogeneous region are still unclear.

Methods: This study investigates the state-level new area Xiong'an New Area and applies the improved enhanced spatial and temporal adaptive reflectance fusion model (ESTARFM) to generated new datasets, which is combined with our previously improved Carnegie–Ames–Stanford approach (CASA) to estimate HANPP. Spatio-temporal variations of HANPP are mapped and assessed using Mann–Kendall (M–K) trend analysis approach from 2000 to 2018 with a high resolution. The relationship among the HANPP, subcomponents, and natural–social–economic-driven factors is discussed herein.

[*] Correspondence: Qianfeng Wang, College of Environment and resource, Fuzhou University, Fuzhou, China. Tel.: +86 131 2317 4301; fax: +86 59122866077; E-mail: wangqianfeng@fzu.edu.cn

Results: The results show that the improved ESTARFM-derived fusion images fitted well with the observed images having the superior correlation coefficient (r), structural similarity index, root mean square error, and mean absolute deviation of 0.75, 0.76, 0.035, and 0.026, respectively, and the normalized difference vegetation index (NDVI) differences are mainly concentrated on the range of 0–0.15 for all months. The HANPP derived by the fusion-based images, above 60% of potential NPP, varied across the whole area, especially between various vegetation types. The HANPP exhibited a significant positive correlation ($r > 0.46$, $P < 0.05$) with precipitation and held an uptrend because of the increase of the harvested HANPP which related with the socio-economic conditions having the determination coefficients above 0.76.

Conclusions: The spatio-temporal fusion contributed to fine spatial patterns and trends of HANPP among various vegetation types. Though the harvested HANPP increased from 2000 to 2018, the agricultural and socio-economic developments did not bring extensive HANPP growth, indicating that the expansion has not violated its sustainable development goal. The results provide a deep insight of the background characteristics in Xiong'an New Area, which has great potential in supporting the future scientific construction of the new area.

Keywords: Spatio-temporal fusion; Mann–Kendall trend analysis; Human appropriation of net primary production; Dynamic; Driven factors

Background

The resources necessary for human development mainly come from the vegetation products or materials in terrestrial ecosystems (Huang et al. 2020). Accompanied with

43 population growth and urbanization, humans have induced great changes in terrestrial
44 ecosystems, which constantly approached upper limits for the terrestrial ecosystems
45 (Running 2012). Over the past 50 years, global agricultural and forestry productions
46 have increased by 30% and 200%, respectively (Godfray et al. 2010; Warman 2014).
47 By 2011, at least 29% of the Earth's surface had been converted into a high-density
48 built-up area, or a high-intensity agricultural land (Ellis 2011). Moreover, global
49 population will reach 9.7 billion, with the urban population accounting for 69%, in the
50 next 30 years, which is expected to lead to a further expansion of 10^9 ha of agricultural
51 lands (Zhou et al. 2018). Therefore, the anthropogenic appropriation from terrestrial
52 ecosystems must be precisely monitored to realize the sustainable development goals
53 (SDG). The human appropriation of net primary production (HANPP) is a
54 comprehensive socioecological indicator coupling human extraction from various
55 vegetation types, which has attracted extensive attention and become one of the widely
56 used methods for assessing sustainable development (Krausmann et al. 2013).

57 Net primary production (NPP) is the key subcomponent of HANPP that refers to
58 the fixed net carbon amount of vegetation per unit area after photosynthesis
59 accumulation and respiration consumption in a certain period (Artacho and Bonomelli
60 2017). NPP is a critical, but limiting natural resource that supports all heterotrophs,
61 including humans (Zhang et al. 2018). Many methods had been developed to simulate
62 both the potential and the actual NPPs in terrestrial ecosystem (Huang et al. 2020). For
63 example, the Miami empirical model (Lieth 1975), light use efficiency-based model
64 (Haberl 1997), and vegetation physiological dynamics process-based model (Haberl et

al. 2007), had all been applied for potential NPP estimation. Meanwhile, the Lund–Potsdam–Jena method (Haberl et al. 2007), Carnegie–Ames–Stanford approach (CASA) (Zhu et al. 2007), and mixed approach (Fetzel et al. 2014), had all been used for the actual NPP simulation. Among these models, the CASA based on remote sensing data showed good efficiency on both potential and actual NPP simulations in a regional scale (Pachavo and Murwira 2014). Our previous study improved the CASA model to simulate the NPP in China during the early 21st century by considering land cover change (Wang et al. 2018).

Spatio-temporal fusion model of remote sensing can provide a cost-effective method for retrieving the NPP across spatio-temporal scales with a fine-resolution (Tang et al. 2020a). As most of remote sensing data are either only available on higher spatial resolution or higher temporal resolution, the compromises between the spatial and temporal resolutions limit detailed, fine-scale accounts of NPP spatial patterns and its dynamics (Tang et al. 2020b). Spatio-temporal fusion model can cope with these resolution tradeoffs by combining the advantages of multi-source remote sensing images and has been developed in heterogeneous regions (Zhu et al. 2010; Zhu et al. 2016; Cheng et al. 2017; Tang et al. 2020a). Fusion images with both high spatial and temporal resolutions have been successfully applied in agriculture production estimation (Liao et al. 2019), forest disturbance monitoring (Schmidt et al. 2015) and urban expansion surveying (Nduati et al. 2019). However, studies integrating the fusion model into NPP simulation in regional scale are still lacking. Therefore, it is necessary

to use the fusion model to sufficiently mine information on remote sensing images and then provide fine datasets for NPP simulation.

HANPP, which is defined as the sum of the NPP harvested via human productive activities and the NPP changed by human-dominated land use conversion (Haberl et al. 2014), has been increasingly used to measure the extent of human domination and transformation of ecosystems (Haberl et al. 2007). Quantifying HANPP can facilitate the understanding of carbon cycling, ecosystem services, and sustainable development, which has triggered considerable attention among global scholars (Huang et al. 2018). Previous studies concentrated more on large spatial scales such as global scale (Haberl et al. 2007; Krausmann et al. 2013; Zhou et al. 2018), continental scale (Fetzel et al. 2016; Plutzar et al. 2016) and national scale (Fetzel et al. 2014; Niedertscheider and Erb 2014; Niedertscheider et al. 2014), while fewer studies have focused on the regional scale (Andersen et al. 2015). However, because of the regional heterogeneity, even the same intensity of human activities can cause various extents of the HANPP in different regions (Zhang et al. 2018). Furthermore, limited by the coarse resolution of calculating data for HANPP, the detailed analysis of HANPP dynamics in a heterogeneous region has not yet been clearly understood. Fine resolution HANPP in a human-dominated heterogeneous region, however, would provide precise spatio-temporal information for the deep evaluation of the region-specific ecological effect (e.g., sustainability), mastering the driven factors and clarifying the impacts of policy making (Erb 2012). Therefore, research should be more detailed and refined on specific region.

Xiong'an New Area is a state-level new area in China that serves to phase out the non-capital functions from Beijing, explore a new model of optimized development in densely populated areas, and restructure the urban layout in the Beijing, Tianjin, and Hebei (BTH) region. As the deputy capital of China, eco-environmental protection and green ecological development in this area are the top priorities (Song et al. 2018). However, the construction of a new area may bring several ecological risks, including reduction of biodiversity, shortage of water resources, and degradation of the ecosystem health (Xu et al. 2013; Song et al. 2018; Xie et al. 2019). Therefore, monitoring and quantifying human interference in Xiong'an New Area can ensure its strategic target of future planning.

In this study, we take the human-dominated Xiong'an New Area, which is a typical heterogeneous region in China, as the study area and aim to demonstrate a detailed spatial pattern and the dynamics of the HANPP from 2000 to 2018. Accordingly, we improved enhanced spatial and temporal adaptive reflectance fusion model (ESTARFM), which has been proven a robust prediction for the time series research in a heterogeneous region (Tang et al. 2020b), to generate time series fusion images with 30 m spatial resolution by blending Landsat Thematic Mapper (TM), Enhanced Thematic Mapper Plus (ETM+), Operational Land Imager (OLI) series with Terra Moderate Resolution Imaging Spectroradiometer (MODIS) MOD09A1 series. The common HANPP framework is utilized to estimate HANPP with a fine spatial resolution based on the fused images (Haberl et al. 2007). The spatial pattern and trend for both the HANPP and its subcomponents are analyzed using the Mann–Kendall (M–

K) trend analysis approach. In addition, the relationship between the HANPP and the natural-, social-, and economic-driven factors is discussed, respectively. The results of this study contribute to the deep understanding of the background characteristics of vegetation in Xiong'an New Area, which will further help in the green development, urban planning, and decision making of the new area.

Materials and methods

Study area

Xiong'an New Area is located in the center of Hebei Province (Fig. 1, 38°43′–39°0′ N, 115°38′–116°20′ E). The agricultural land in Xiong'an New Area accounted for more than half of the total area in 2016 (Tang et al. 2020b). The new area construction will expand the region from 1566 km^2 to 2000 km^2 in the future (Xu et al. 2018). Winter wheat and summer corn are the major crops in this area (Wang et al. 2017a; Wang et al. 2017b), and there are both ripe once a year and ripe twice a year for agriculture (Tang et al. 2020b). Xiong'an New Area has a warm temperate monsoon continental climate with the annual temperature and precipitation of 12.1 °C and 560 mm, respectively (Xu et al. 2018). Human interferences generally concentrate on agriculture production and urban construction.

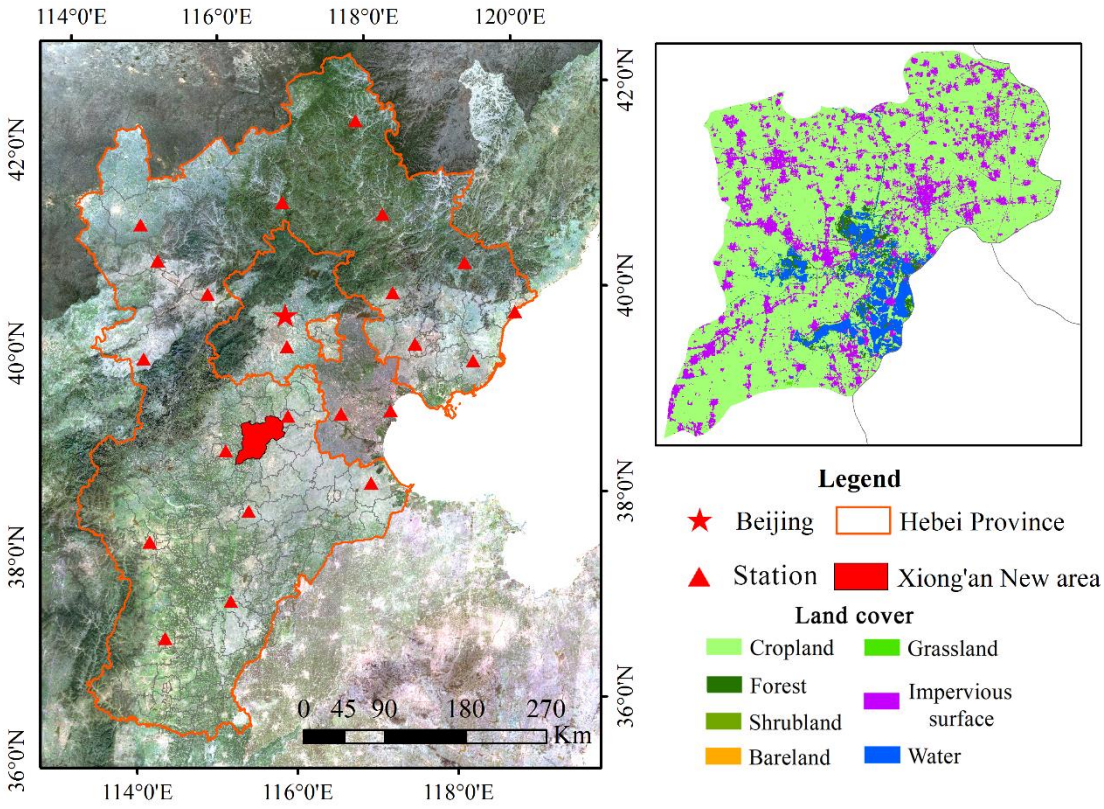

Fig. 1. Location and land cover map of Xiong'an New Area

Datasets and processing

The remote sensing, land use, meteorological station, and economic statistic data were all integrated into the HANPP framework (Table 1). The remote sensing data covered the atmospherically corrected surface reflectance products of Landsat TM/ETM+/OLI and the MOD09A1 products of Terra MODIS (Collection 6). All products were collected and preprocessed in the Google Earth Engine platform. The preprocessing mainly included two steps: 1) calibration between TM/ETM+ and OLI to document the sensor differences and generate the temporal continuous reflectance data in the study period according to the previous study (Roy et al. 2016); and 2) georeferencing between Landsat and MODIS to meet the input requirement of the ESTARFM method (Zhu et al. 2010). The meteorological data included daily

temperature, daily precipitation, and daily sunshine duration from 22 national meteorological stations in the BTH region. All data were converted into month data by summing up or averaging the daily data in each month at each station. The monthly total solar radiation was calculated based on the daily sunshine duration data (Wang et al. 2017a). All station data were interpolated into rasters, consistent with the remote sensing data, through the Inverse Distance Weighted method. The economic statistic data covered 12 kinds of main crops and wood harvested data, agricultural condition data, and social–economic data. The harvested data were available only for political units and did not match the remote sensing data. Hence, we assumed the same crop (wood) yield per unit of cropland (forest) in Xiong'an New Area and distributed the yield to each pixel based on the land cover map (Li and Meng 2018). We also collected three phases of land cover product data with 30 m spatial resolution in Xiong'an New Area.

Table 1. Data sources for HANPP framework input.

Data	Feature	Range	Source	Use
Remote sensing data	TM, ETM+, OLI, MOD09A1	2000-2018	Google Earth Engine platform	NPP
Meteorological station data	temperature, precipitation, sunshine duration	2000-2018	China Meteorological Administration (http://data.cma.cn/en)	NPP
Economic statistic data	Food crop (rice, wheat, maize, etc.), Economic crop (Peanuts, sesame, cotton vegetables, fruits, etc.), wood, GDP, fertilizer, non-agricultural population, available irrigated area	2000-2018	Economic Statistics Yearbook of Baoding city	$HANPP_{harv}$
Land cover data	Land use	2010, 2015, 2017	Tsinghua University (http://data.ess.tsinghua.edu.cn/)	NPP

Methods

Improved ESTARFM algorithm

The original ESTARFM used two pairs of Landsat-MODIS images to generate images with fine spatio-temporal resolution, and was effective in heterogeneous areas (Knauer et al. 2016; Zhu et al. 2010). The algorithm was operated on pixel level, and the reconstruction of each target pixel was based on several similar pixels, having the minimal spectral differences to the target pixel, which were selected by setting a constant threshold in the fine Landsat images (Equation (1)). Based on the selected similar pixels, the spatial, spectral and temporal weights of each similar pixel were calculated and normalized and the conversion coefficient of each target pixel was

198 calculated through linear regression to transfer the MODIS pixel changes into the
199 Landsat scene at the prediction date. Take the neighboring effects into consideration,
200 the similar pixels were selected in a moving window to eliminate the block effect. The
201 final reflectance value of the target pixel could be calculated by (Equation (2)).

202 $$\left|F\left(x_i, y_j, t_m, B\right) - F\left(x_{w/2}, y_{w/2}, t_p, B\right)\right| \le \sigma\left(B\right) \times 2/c \quad (1)$$

203 F, B, c, σ represent the Landsat image, bands, class number and the standard
204 deviation respectively. $\left(x_i, y_j\right)$ and $\left(x_{w/2}, y_{w/2}\right)$ are the position of similar pixels and the
205 target pixel of the moving window, respectively. t_p represents the predicted date, t_m
206 represents the observed date.

207 $$F\left(x_{w/2}, y_{w/2}, t_p, B\right) = F\left(x_{w/2}, y_{w/2}, t_m, B\right) + \sum_{i=1}^{N} W_i \times V_i \times \left(C\left(x_i, y_i, t_p, B\right) - C\left(x_i, y_i, t_m, B\right)\right) \quad (2)$$

208 Here, W_i, V_i, N indicate the normalized weight, conversion coefficient and the
209 number of selected similar pixels, respectively. More information can be found in (Zhu
210 et al. 2010).

211 However, one basic assumption of the algorithm was the linearly changed reflectance
212 during a short time period, which may go against the non-linear phenological variation
213 during the actual growth cycle (Tang et al. 2020a). Furthermore, the precise of selected
214 similar pixels have the determined impact on the final predicted images, however, the
215 constraints of selection based the two phases of fine Landsat images may not enough
216 for time series prediction. For example, better results would be obtained when the
217 Landsat images at t_m and t_n were in the same growth stages and the predicted image
218 at t_p was between t_m and t_n. But the worse results were generated when the input

Landsat images have the different growth stages (Tang et al. 2020a). Therefore, we improved the original approach by adding extra input Landsat image to filter out the false similar pixels. Three pairs input images, before, during and after the crop vegetation growth, can also represent the annual growth cycle and have the robust effect for time series fusion according to our previous study (Tang et al. 2020b).

HANPP framework

In this study, the HANPP followed the widely defined framework used in the previous study, which calculated the HANPP as follows (Haberl et al. 2007; Andersen et al. 2015).

$$HANPP = NPP_{pot} - \mathrm{NPP}_{act} + HANPP_{harv} \quad (3)$$

where, NPP_{pot}, NPP_{act}, $HANPP_{harv}$ represent the potential, actual and harvested NPPs, respectively. NPP_{pot} indicates the amount of NPP provided by the ecosystem without human disturbance, while NPP_{act}, $HANPP_{harv}$ indicate the actual NPP in a real ecosystem condition and the harvested NPP via human activities, respectively.

The potential and actual NPPs were calculated using our improved CASA model, which was further calibrated by field observed data in China (Zhu et al. 2007), and considered the land cover change (Wang et al. 2018). The improved CASA model thought that the NPP comprised absorbed photosynthetically active radiation (APAR) and light utilization efficiency (ε).

$$NPP = APAR_{(x,t)} * \varepsilon_{(x,t)} \quad (4)$$

where, x, t denote the spatial position and the time, respectively, and $APAR_{(x,t)}$ is derived as follows.

$$APAR_{(x,t)} = SOL_{(x,t)} * FPAR_{(x,t)} * 0.5 \quad (5)$$

where, $SOL_{(x,t)}$ represents total solar radiation at position x and time t, and $FPAR_{(x,t)}$ indicates the absorption ratio of the solar radiation. The constant (0.5) represents that only half of the total solar radiation from the Sun can be useful for vegetation (wavelength: 0.4 μm to 0.7 μm). $FPAR_{(x,t)}$ and $\varepsilon_{(x,t)}$ can be further calculated based on the previous study (Wang et al. 2018). Meanwhile, considering the human interference on cropland and built-up land, we adjusted the CASA model parameters for these two land cover types to calculate the potential NPP according to Hua's research (Hua 2009).

The harvested NPP was made of the NPP derived from the cropland, built-up land, and forest. The cropland-harvested NPP included the edible and crop residue part. Both parts were converted into the carbon content value using the method in Zhang's study, which was based on the crop's statistical yield, straw coefficient, dry matter fraction, carbon fraction, and recover rate (Zhang et al. 2015). These crop-specific parameters could be obtained from former studies (Table 2) (Haberl et al. 2007; Huang et al. 2007; Xie et al. 2011; Wang et al. 2012).

Table 2 Straw coefficient, dry weight fraction, carbon fraction and recovery rate of main crops

Crop	Straw coefficient	Dry matter fraction	Carbon fraction of edible part	Carbon fraction of edible part	Recover rate
Rice	0.95	0.85	0.38	0.42	0.2
Wheat	1.22	0.85	0.39	0.49	0.2
Maize	1.05	0.78	0.39	0.47	0.2
Sorghum	1.6	0.91	0.45	0.45	0.2
Soybean	1.36	0.85	0.40	0.45	0.5
Potato	0.42	0.20	0.39	0.42	0.25

Batata	0.53	0.20	0.39	0.42	0.25
Peanut	0.86	0.885	0.38	0.38	0.2
Rape	2.57	0.90	0.42	0.45	0.3
Sesame	1.78	0.85	0.40	0.45	0.2
Cotton	2.62	0.90	0.40	0.39	0.2
Vegetable	0.1	0.1	0.475	0.475	0.2
Fruit	0.15	0.15	0.475	0.475	0.2

We assumed that the forest-harvested NPP was sourced from the timber yield. The corresponding carbon contents were calculated based on the wood density and carbon fraction derived from Haberl's study (Haberl et al. 2007). Meanwhile, the NPP values were calculated as the timber yield multiplied by wood density and carbon fraction. Considering the data availability, we took half of the actual NPP as the built-up land-harvested NPP according to the former study (Fetzel et al. 2014).

Trend analysis method

In this study, M–K was utilized to demonstrate the spatial trend of both the HANPP and its subcomponents (Mann 1945). M–K is one of widely used nonparametric test methods in the field of meteorology, ecology, and agriculture (Burn and Elnur 2002; Xu et al. 2004). The M-K test statistic was calculated as follows:

$$S = \sum_{k=1}^{n-1} \sum_{j=k+1}^{n} \operatorname{sgn}\left(x_j - x_i\right) \tag{6}$$

where x_i, n represent the data sequence value and length, respectively, and sgn is calculated as follows:

$$sgn(x_j - x_i) \begin{cases} 1 & \text{if } x_j > x_i \\ 0 & \text{if } x_j = x_i \\ -1 & \text{if } x_j < x_i \end{cases} \tag{7}$$

Based on the M–K test theory, S followed a normal distribution when n was larger than 8. The S expectation and variance are expressed as the follows:

277 $$E(S)=0 \quad (8)$$

278 $$V(S)=\frac{n(n-1)(2n+5)-\sum_{m=1}^{n} t_m m(m-1)(2m+5)}{18} \quad (9)$$

279 where, t_m is the value of extent m. Therefore, the normalized test statistics Z could

280 be derived as the follows:

281 $$Z=\begin{cases}\frac{S-1}{\sqrt{V(S)}} & S>0\\ 0 & S=0\\ \frac{S+1}{\sqrt{V(S)}} & S<0\end{cases} \quad (10)$$

282 When $|Z|$ was lager than 1.65, 1.98, and 2.58, the trend had significant levels (p)

283 corresponding to 0.1, 0.05, and 0.01, respectively. To further understand the trend

284 magnitude, we applied the robust trend estimator developed by Sen (1968) to calculate

285 the trend slope as follows (Sen and Kumar 1968).

286 $$slope=Median\left(\frac{x_j-x_i}{j-i}\right)(1\le i<j\le n) \quad (11)$$

287 where, slope indicates the monotonic increase (positive) or decrease rate (negative) of

288 the data sequence.

289 **Results**

290 **Generation of time series fusion images**

291 We obtained six-band (i.e., blue, green, red, NIR, SWIR1, and SWIR2) time series

292 monthly fusion images from 2000 to 2018 based on the improved ESTARFM approach.

293 Multiple testing indicators, including correlation coefficient (r), root mean square error

294 (RMSE), structural similarity index (SSIM), and mean absolute deviation (MAD), were

295 used to validate the accuracy of the fusion images. The box plot in Fig. 2 shows that all

296 the indicators were distributed in the 1.5 times inter-quartile range (1.5 * IQR), except

for only few data points, in SWIR1 and SWIR2 band, exhibited abnormalities. Furthermore, most data points especially concentrated inside the box (25th to 75th percentile). The average values of r and SSIM were above 0.75 and 0.76, respectively, while those of the RMSE and MAD were lower than 0.035 and 0.026, respectively. Among the six spectral bands, the testing results of the red and NIR bands, which were sensitive to the vegetation, had better accuracies with r and SSIM of up to 0.8 and 0.79, respectively, and RMSE and MAD of up to 0.022 and 0.017, respectively.

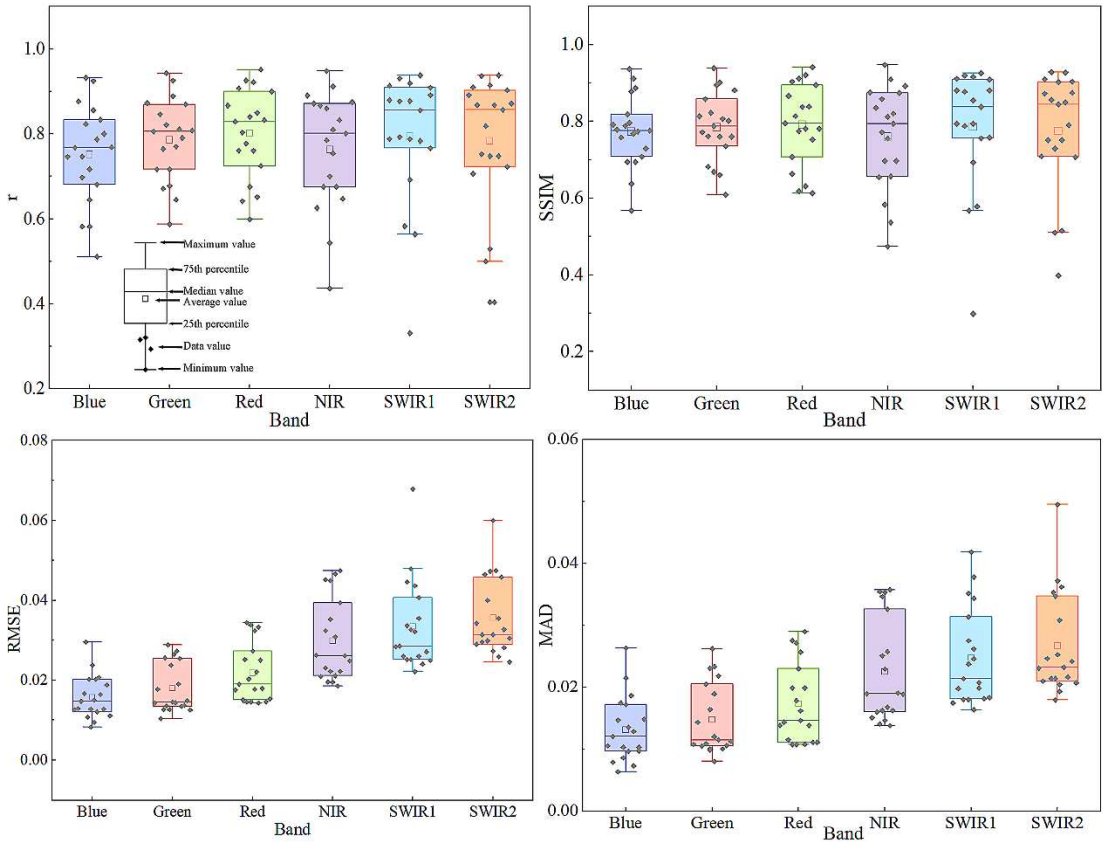

Fig. 2 Accuracy of multiple indicators for the fusion images from 2000 to 2018: (a) r, (b) SSIM, (c) RMSE, and (d) MAD

We calculated the NDVI differences (ΔNDVI) between the NDVI based on the fusion images and that based on the observed images to further verify the accuracy of

the NDVI derived from the fusion images. Compared with the monthly NDVI images from 2000 to 2018 (Fig. 3), ΔNDVI for all months were mainly concentrated in the range of 0–0.15. Moreover, the differences in February, August, and September were better than those of the other months with 1.5 * IQR less than 0.1. The average differences of February, August, and September were 0.05, 0.04, and 0.03, respectively.

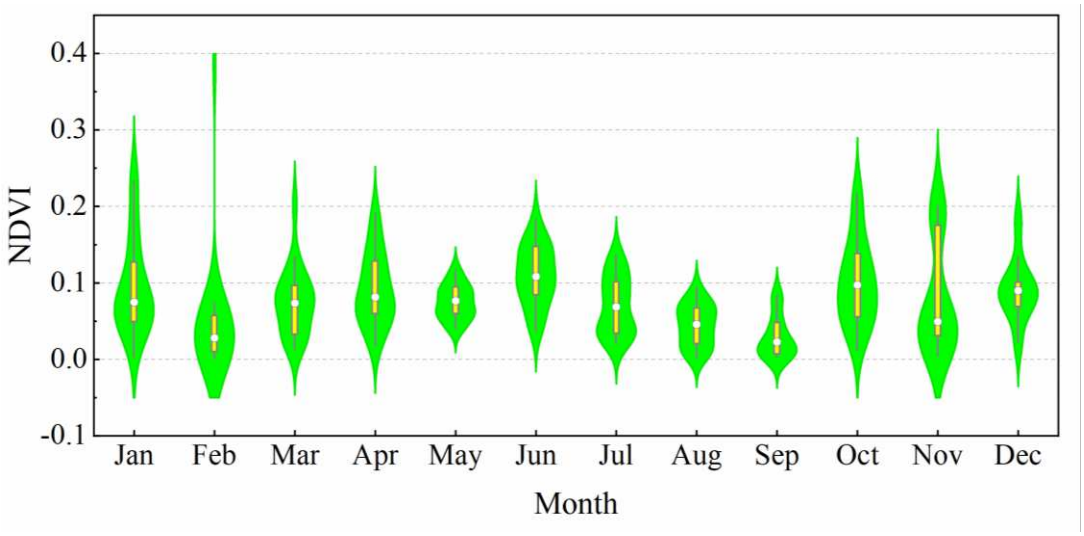

Fig. 3 ΔNDVI distribution of each month from 2000 to 2018

Change of subcomponents and HANPP

According to the abovementioned methods, we could obtain the dynamics of both the HANPP and its subcomponents based on the fusion images (Fig.4). Fig. 4(a) depicts that NPP_{pot} and NPP_{act} exhibited fluctuating changes, while $HANPP_{harv}$ showed a slight increase in change from 2000 to 2018. Meanwhile, Fig. 4(b) demonstrates that the HANPP was larger than 670 g·C/m^2, and HANPP% NPP_{pot} was above 60%.

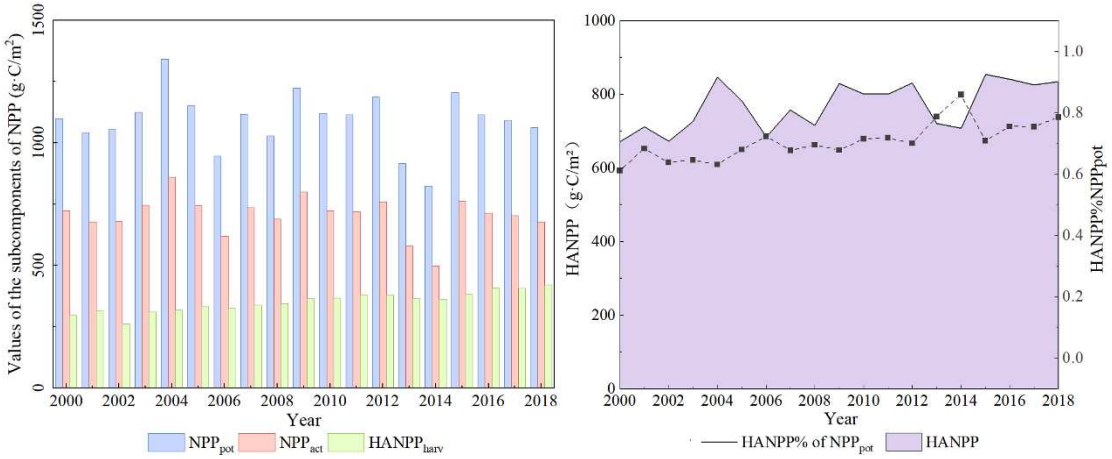

Fig. 4 Change of the HANPP and its subcomponents and the ratio to NPP_{pot}: (a) subcomponents and (b) HANPP

Fig. 5 displays the spatial trends and the corresponding significant level (P-value), of the three HANPP subcomponents. NPP_{pot} and NPP_{act} had similar change laws of the increasing trend occurring in the southern and northeastern Xiong'an New Area and the decreasing trend concentrating in the middle area (Figs. 5(a) and (b)). However, both uptrend and downtrend showed non-significant levels. $HANPP_{harv}$ displayed an increasing trend in the total area, except for the southeastern area covered in water and unsuitable for agriculture or urban construction (Fig. 5(c)). The uptrends had a very significant level ($P < 0.01$).

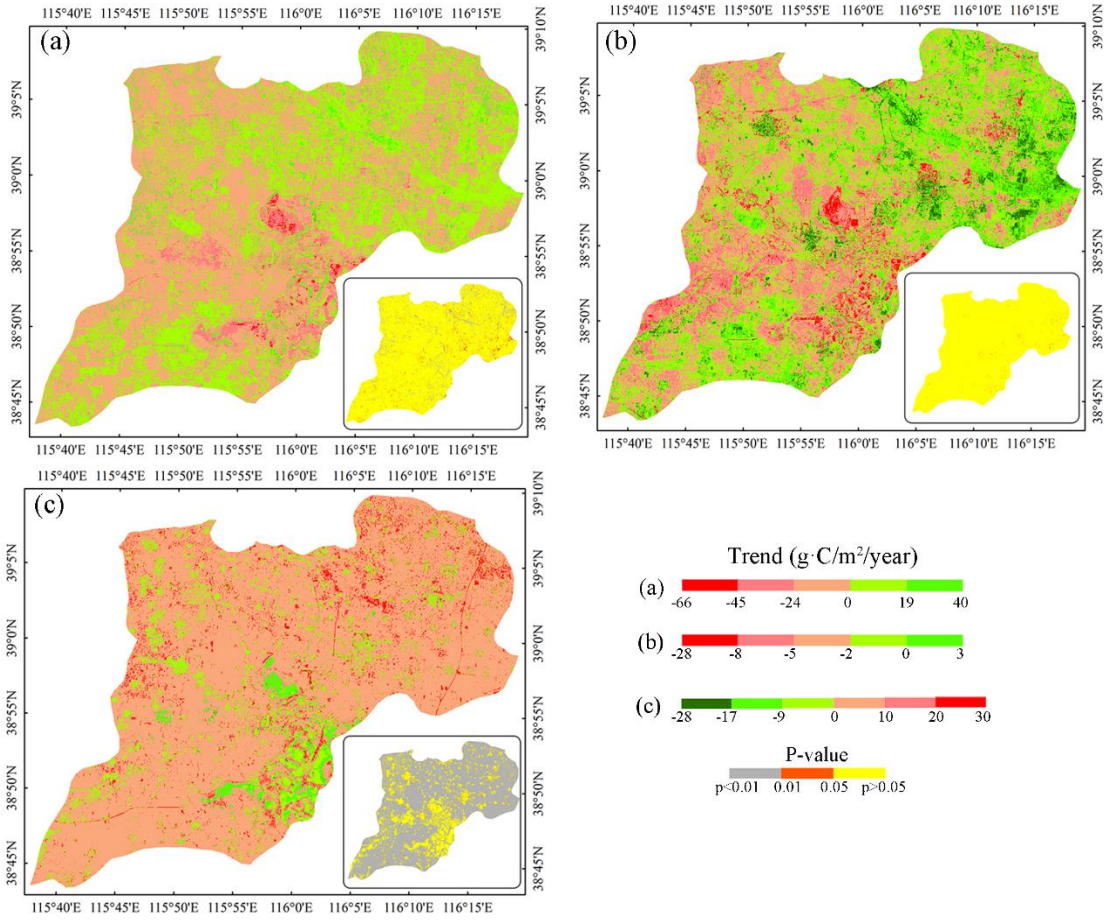

Fig. 5 Spatial trend and corresponding significant level of the HANPP subcomponents: (a) NPP_{pot}; (b) NPP_{act}; and (c): $HANPP_{harv}$

Spatial pattern and trend of the HANPP

We obtained the HANPP spatial pattern (Fig. 6) based on the results of NPP_{pot}, NPP_{act}, and $HANPP_{harv}$ and found that the HANPP varied across the whole area. The highest HANPP level emerged in the region with a longitude between the 115°40′E and 116°E, while the higher HANPP levels prevailed with a latitude increase. Some built-up and the water areas held a relatively low HANPP of less than 500 g·C/m^2 as a consequence of low agricultural intensity.

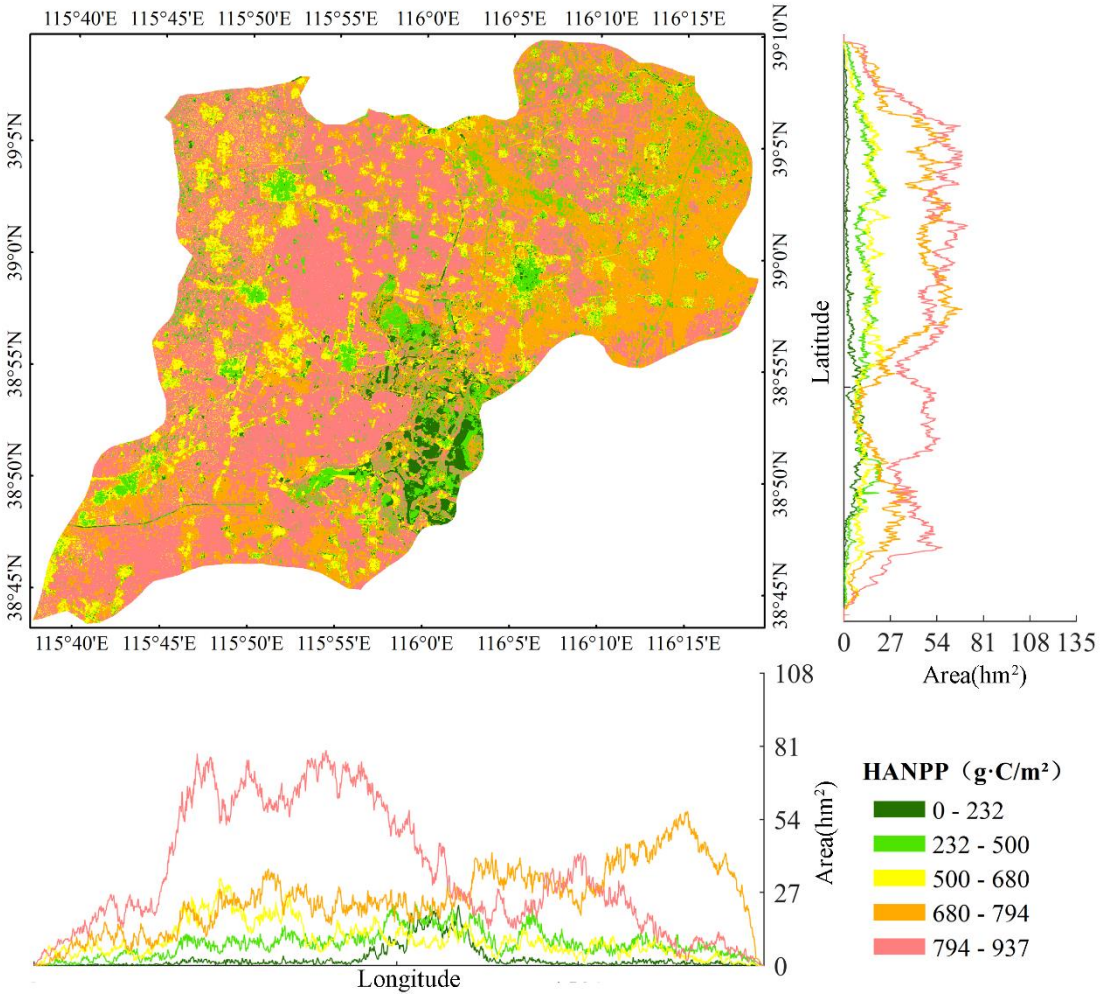

Fig. 6 Spatial pattern of the HANPP in Xiong'an New Area

Fig. 7 demonstrates the spatial trend of HANPP, from which we found most of the regions showed an increasing trend with a magnitude of less than 22 g·C/(m^2·year), while the southeastern area and some discreted western area had a decreasing trend. Both along with the latitude and longitude, the trends held an increasing change (0-22 g·C/(m^2·year)) from 2000 to 2018. The trend expressed an extremely significant level ($P < 0.01$) in the northeastern and southern areas and a significant level ($P < 0.05$) in the middle and northwestern regions. In contrast, a non-significant level was observed in the southeastern area.

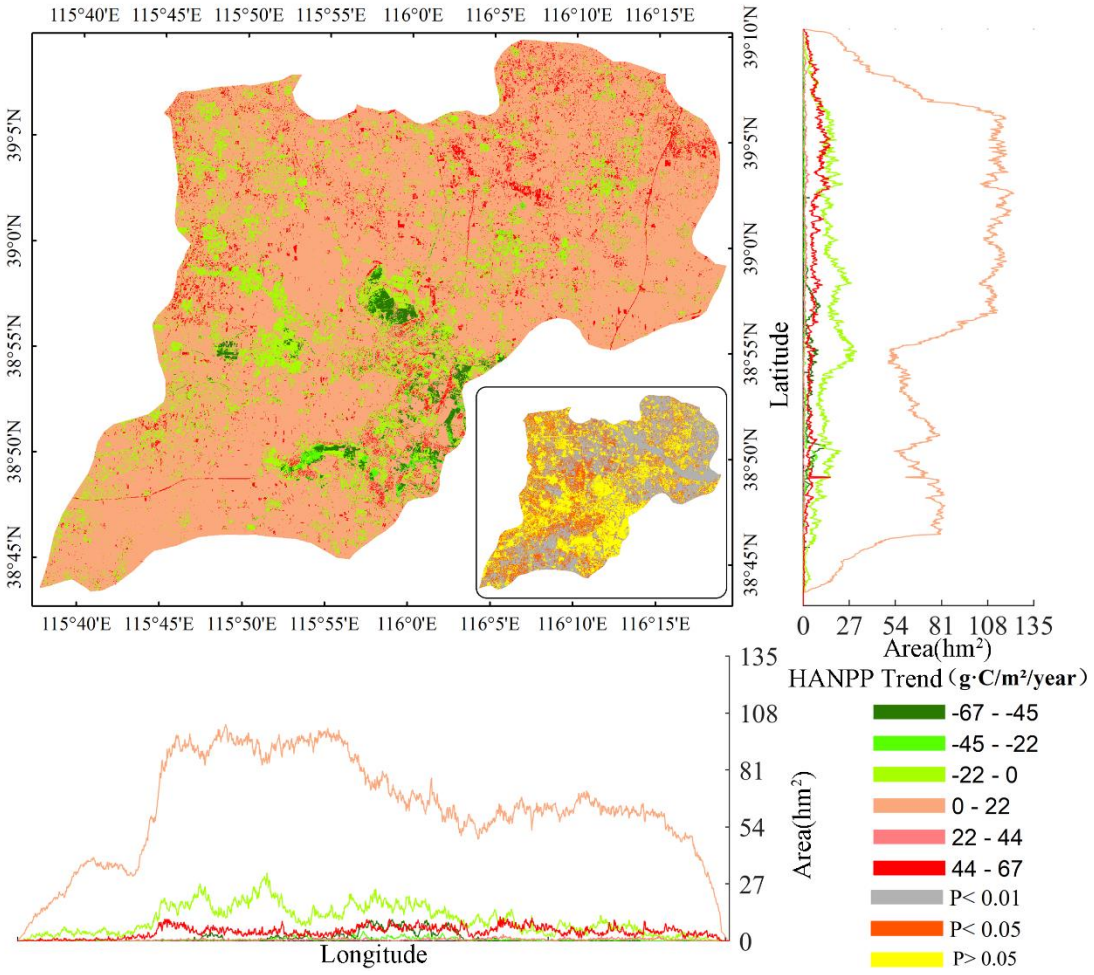

Fig. 7 Spatial trend of the HANPP in Xiong'an New Area

Discussion

Correlation between climate factors and the HANPP

Temperature and precipitation are two climate factors related to the geographical distribution of vegetation, which are important to the NPP in a dryland ecosystem (Wang et al. 2019). Among all climate factors, precipitation has the greatest influence on the vegetation cover changes (Zhou et al. 2019), is further related to the crop yield in the Hebei region (Wang et al. 2020). In this study, we mapped the spatial correlation between temperature, precipitation and HANPP at pixel level based on the meteorological raster data. According to Fig. 8(a), the HANPP showed a low correlation

with temperature across most parts of Xiong'an New Area, with the correlation coefficient ranging from −0.39 to 0.39 and the significant level $P > 0.1$. These results reflected the same phenomenon of the NPP being not significantly correlated with the average annual temperatures in Hebei (Wang et al. 2018). From Fig. 8(b), we concluded that HANPP in most cropland region held the significant correlation with precipitation, whose coefficients were larger than 0.46 ($P < 0.05$). The results was consistent with the previous study that precipitation played main role in crop yields or harvested HANPP (Wang et al. 2017a). Since the precipitation was closely linked to latitude in Hebei (Zhao et al. 2018), even larger correlation coefficient (>0.58) with an extremely significant level ($P<0.01$) were observed on the northern cropland. Notably, the correlation was regarded as extremely and significantly negative because some regions in southeastern Xiong'an New Area were always covered by water from 2000 to 2018, causing them to lack human appropriation.

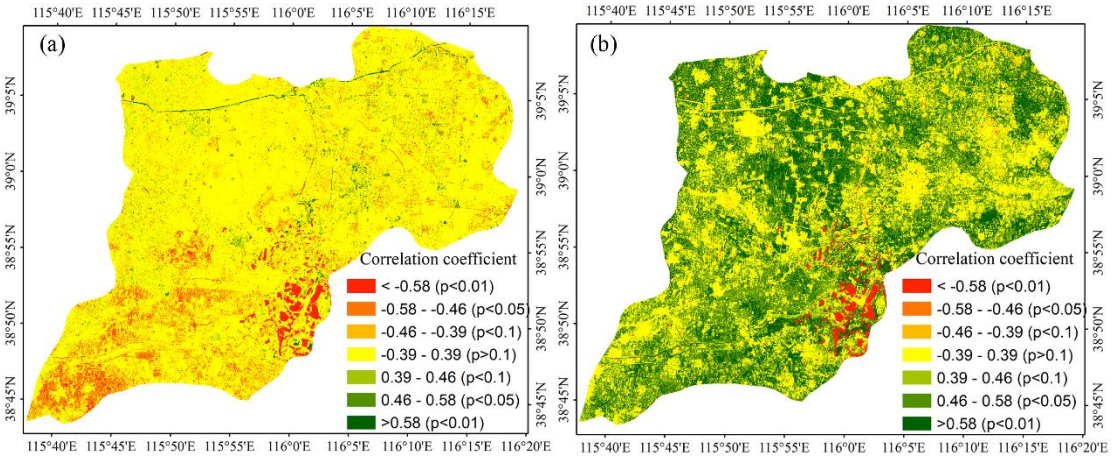

Fig. 8 Correlation between climate factors and the HANPP in Xiong'an New Area: (a) temperature and (b) precipitation

Influences of agricultural conditions on the HANPP

391 Agriculture dominates in Xiong'an New Area; hence, agricultural conditions may
392 play an important role in the HANPP dynamics. A previous study identified fertilizer
393 use and irrigation area as two main agricultural-driven factors for the determination of
394 the HANPP amount (Krausmann et al. 2012). Therefore, we also analyzed herein the
395 driving relationship between these agricultural conditions (i.e., amount of fertilizer and
396 available irrigated area) with the HANPP elements (i.e., $HANPP_{harv}$ and HANPP). Figs.
397 9(a)–(c) depict that $HANPP_{harv}$ and HANPP responded to the amount of fertilizer with
398 determination coefficients (R^2) equal to 0.59 and 0.22, respectively. These results
399 indicate that fertilizer use could prompt the agricultural production to some extent. The
400 conclusions were similar to those obtained for the same agricultural ecosystem in the
401 coastal areas of Jiangsu (Zhang et al. 2015). However, note that the change of the
402 available irrigated area had a low influence on the HANPP elements ($R^2 < 0.04$) because
403 even a limited irrigation could achieve a relatively high agricultural production through
404 the enhanced water use efficiency (Xu et al. 2016). The irrigation capacity was no
405 longer the main limiting factor on production in Xiong'an New Area as a consequence
406 of the developed agriculture technology.
407

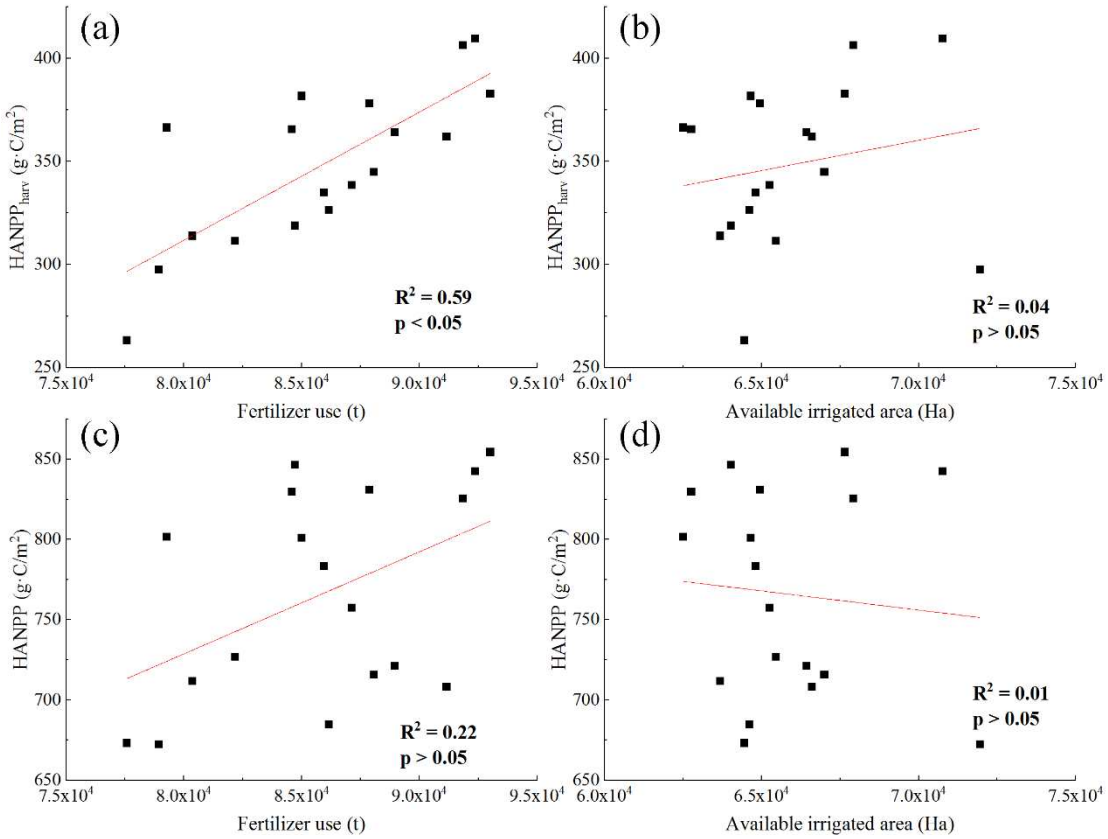

Fig. 9 Correlation of agricultural conditions with the HANPP elements: (a) fertilizer use and HANPP$_{harv}$; (b) available irrigated area and HANPP$_{harv}$; (c) fertilizer use and HANPP; and (d) available irrigated area and HANPP

Influences of socio-economic conditions on the HANPP

HANPP integrates socio-economic conditions with natural dimensions, which demonstrate a positive correlation with a region's population (Krausmann et al. 2012; Erb et al. 2013). Accompanied by urbanization and economic development, especially after the proposal of the Xiong'an New Area construction, how socio-economic conditions are related to the HANPP should be mastered. The per capita GDP (yuan per person) and the fraction of the non-agricultural population were selected herein as the socio-economic indicators for analyzing the HANPP element response to these factors in Xiong'an New Area. (Niedertscheider et al. 2017). We conclude that both the per

capita GDP and the fraction of the non-agricultural population had a relatively low impact on the HANPP, with R^2 equal to 0.24 and 0.41, respectively (Fig. 10). The small R^2 also demonstrated that the construction and the development of Xiong'an New Area would not bring extensive growth of human appropriation on the ecosystem and violate its SDG. However, human occupation on the built-up area would increase because of the forthcoming urban expansion and population growth (Xu et al. 2018). Therefore, R^2 between per capita GDP and $HANPP_{harv}$ (0.76), fraction of the non-agricultural population and $HANPP_{harv}$ (0.86) reflected the great relationship of social development to human-harvested NPPs.

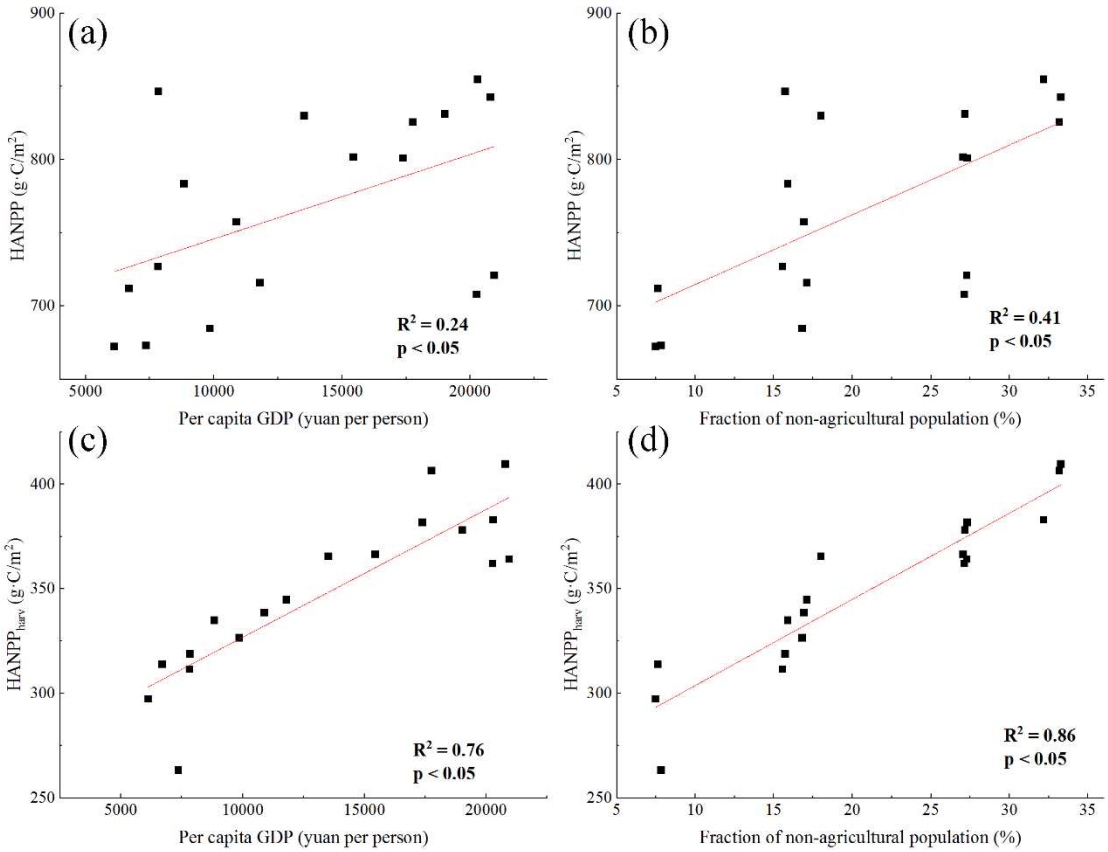

Fig. 10 Correlation between the socio-economic conditions and the HANPP elements: (a) per capita GDP and HANPP; (b) fraction of the non-agricultural population and the HANPP; (c) per capita GDP and $HANPP_{harv}$; and (d) fraction of the non-agricultural population and $HANPP_{harv}$

435 **Comparison with previous studies on the HANPP**

436 The HANPP%NPP_{pot} proportion is a comparable indicator for assessing the level
437 of appropriated NPP by human activities among different countries and regions (Huang
438 et al. 2020). Table 3 shows that reports in different study areas had distinct
439 HANPP%NPP_{pot} results, which, on the one hand, may be caused by the different
440 definitions of and calculation methods for the HANPP (Haberl et al. 2007), and on the
441 other hand, may be caused by the heterogeneity of the study area to a large extent
442 (Andersen et al. 2015). Our study, which considered human extraction from cropland,
443 built-up land, and forest, obtained HANPP%NPP_{pot} values ranging from 62% to 82%.
444 These results were higher than those obtained from research in the coastal areas of
445 Jiangsu, the similar agricultural dominated region that only considered the cropland-
446 harvested NPP (Zhang et al. 2015). However, our results were consistent with those
447 acquired for some developed Europe countries, including United Kingdom, Hungary,
448 and Italy, which have a large proportion of cropland and a high level of agricultural
449 modernization (Kohlheb and Krausmann 2009; Musel 2009; Niedertscheider and Erb
450 2014).

451

452 Table 3 Comparisons between the estimates of the HANPP rate in this study and those in the
453 previous studies

Reference	Scale	Year	HANPP%NPP_{pot}
this study	Xiong'an New Area (China)	2000-2018	62-82
(M. et al. 1986)	Global	1970s	30.7
(Haberl et al. 2007)	Global	2000	23.8
(Haberl et al. 2001)	Austria	1950-1995	51
(Kastner 2009)	Philippines	1910-2003	35-62
(Kohlheb and Krausmann	Hungary	1961-2005	67-49

2009)			
(Musel 2009)	United Kingdom	1800-2000	71-68
(Schwarzlmuller 2009)	Spain	1955-2003	67-61
(Niedertscheider and Erb 2014)	Italy	1884-2007	78-56
(Niedertscheider et al. 2012)	South Africa	1961-2006	21-25
(Chen et al. 2015)	China	2001-2010	49.5-57.8
(O'Neill et al. 2007)	Nova Scotia (Canada)	1999-2003	25.5
(Zhang et al. 2015)	Coastal areas of Jiangsu (China)	2000-2010	50.3-71
(Li and Meng 2018)	Heihe River basin (China)	2001-2013	38-71
(Huang et al. 2020)	Yangtze River Delta	2005-2015	59-72

Impacts, limitations and future work

HANPP accounted both the loss and harvested part of NPP caused by human development, which served as a feasible evaluating tool for regional SDG (Bishop et al. 2010; Ha et al. 2012). Our improved HANPP estimation and dynamics simulation for a long time series could further sustain the scientific construction of the new area. For example, the 30 m spatial resolution HANPP could help us master the spatial pattern of HANPP%NPP_{pot} in a fine grid level, from which we could determine how the high or low values are distributed (a distribution map). Since the higher HANPP%NPP_{pot} meant the less fraction of NPP supported by other species (Haberl et al. 2004), the new area construction should fully consider the distribution map. Meanwhile, NPP loss (NPP_{luc}) caused by human induced land cover change (NPP_{pot} minus NPP_{pot}) could also be calculated in fine grid level and compared with $HANPP_{harv}$. Furtherly, the higher (NPP_{luc}< $HANPP_{harv}$) or lower (NPP_{luc}> $HANPP_{harv}$) land use efficiency would provide scientific instruction for precise agriculture.

In this study, although we made full use of Google Earth Engine Platform for the long time series image collection and preprocessing, the improved ESTARFM method

was time-consuming, especially in the larger region. We have not test the algorithm for HANPP simulation in a large region (e.g., a province). Therefore, these kinds of research should be enriched in the future.

Conclusion

In this study, the improved ESTARFM was applied to generate time series images with a high spatial resolution. These time series images were further used to calculate the HANPP in Xiong'an New Area from 2000 to 2018. Validated by multiple indicators, the improved results contributed to the analysis of the spatial pattern and trend of the HANPP in Xiong'an New area, from which, we concluded that the whole area had the HANPP level higher than 680 $g \cdot C/m^2$. However, some built-up and water areas hold a relatively low HANPP of less than 500 $g \cdot C/m^2$.

Most of the regions showed an increasing trend with a magnitude of less than 22 $g \cdot C/(m^2 \cdot year)$, while the southeastern area and some discrete western areas exhibited a decreasing trend. The trend in the northeastern and south areas expressed a very significant level ($P < 0.01$) and a significant level ($P < 0.05$) in the middle and northwestern regions.

By discussing the correlation between natural, social, economic factors and HANPP, we found that the correlation between the HANPP and the temperature had a low value (−0.39–0.39) with non-significant level ($P > 0.1$) that occurred across the whole Xiong'an New Area. Meanwhile, the HANPP responded to precipitation with a correlation coefficient above 0.46 and a significant level of $P < 0.05$ in most cropland regions. Fertilizer use could prompt both $HANPP_{harv}$ and HANPP to some extent. Both

493 the per capita GDP and the fraction of the non-agricultural population had a high impact
494 on $HANPP_{harv}$ with R^2 equal to 0.76 and 0.86. However, the construction and
495 development of Xiong'an New Area do not go against its sustainable development.

496 **Abbreviations**

497 NPP: Net primary production; HANPP: Human appropriation of net primary
498 production; ESTARFM: Enhanced spatial and temporal adaptive reflectance fusion
499 model; CASA: Carnegie–Ames–Stanford approach; M–K: Mann–Kendall trend
500 analysis approach; NDVI: Normalized Difference Vegetation Index; BTH: Beijing,
501 Tianjin, and Hebei; NPP_{pot}, NPP_{act}, $HANPP_{harv}$: potential, actual and harvested NPPs,
502 respectively.

503 **Acknowledgments**

504 We greatly appreciate the valuable comments from editor and reviewers that helped us
505 to improve the quality of this paper.

506 **Authors' contributions**

507 Jia Tang makes substantial contributions to data acquisition, processing and analysis as
508 well as drafting and critically revising of the manuscript. Qianfeng Wang contributes to
509 the development of ideas and experimental instruction as well as revision of all stages
510 and takes intellectual responsibility for its content. Other authors participate in data
511 processing and technical support of the manuscript.

512 **Funding**

513 This research received financial support from the National Natural Science Foundation
514 of China (No. 41601562) and China Scholarship Council.

Availability of data and materials

Both the original data and processed data are available upon request. All methods/or models used herein can be obtained by contacting the corresponding author.

Ethics approval and consent to participate

Not applicable.

Consent for publication

Not applicable.

Competing interests

The authors declare that they have no competing interests.

Authors' information

[1] Fujian Provincial Key Laboratory of Remote Sensing of Soil Erosion and Disaster Protection/College of Environment and Resources, Fuzhou University, Fuzhou 350116, China

[2] State Key Laboratory of Remote Sensing Science, Aerospace Information Research Institute, Chinese Academy of Sciences, Beijing 100094, China

[3] Joint Global Change Research Institute, University of Maryland, College Park, MD 20740, USA

Reference

Andersen C, Donovan R, Quinn J (2015) Human Appropriation of Net Primary Production (HANPP) in an Agriculturally-Dominated Watershed, Southeastern USA. Land 4: 513-40

Artacho P, Bonomelli C (2017) Net primary productivity and allocation to fine-root production in field-grown sweet cherry trees under different soil nitrogen regimes. Sci. Hortic. 219: 207-15

Bishop JDK, Amaratunga GAJ, Rodriguez C (2010) Quantifying the limits of HANPP and carbon emissions which prolong total species well-being. Environ. Dev. Sustain. 12: 213-31

Burn DH, Elnur MAH (2002) Detection of hydrologic trends and variability. J. Hydrol. 255: 107-22

Chen A, Li R, Wang H, He B (2015) Quantitative assessment of human appropriation of aboveground net primary production in China. Ecol Modell 312: 54-60

Cheng Q, Liu H, Shen H, Wu P, Zhang L (2017) A Spatial and Temporal Nonlocal Filter-Based Data Fusion Method. IEEE Trans Geosci Remote Sens 55: 4476-88

Ellis EC (2011) Anthropogenic transformation of the terrestrial biosphere. Philos. Trans. Royal Soc. A 369: 1010-35

Erb KH (2012) How a socio-ecological metabolism approach can help to advance our understanding of changes in land-use intensity. Ecological Economics 76: 8-14

Erb KH, Haberl H, Jepsen MR, Kuemmerle T, Lindner M, Muller D, Verburg PH, Reenberg A (2013) A conceptual framework for analysing and measuring land-use intensity. Curr Opin Environ Sustain 5: 464-70

Fetzel T, Gradwohl M, Erb KH (2014) Conversion, intensification, and abandonment: A human appropriation of net primary production approach to analyze historic land-use dynamics in New Zealand 1860-2005. Ecological Economics 97: 201-8

Fetzel T, Niedertscheider M, Haberl H, Krausmann F, Erb KH (2016) Patterns and changes of land use and land-use efficiency in Africa 1980-2005: an analysis based on the human appropriation of net primary production framework. Regional Environmental Change 16: 1507-20

Godfray HCJ, Beddington JR, Crute IR, Haddad L, Lawrence D, Muir JF, Pretty J, Robinson S, Thomas SM, Toulmin C (2010) Food Security: The Challenge of Feeding 9 Billion People. Science 327: 812-8

Ha W, Gowda PH, Howell TA (2012) A review of downscaling methods for remote sensing-based irrigation management: part I. Irrig Sci 31: 831-50

Haberl H (1997) Human Appropriation of Net Primary Production as an Environmental Indicator: Implications for Sustainable Development. Ambio 26: 143-6

Haberl H, Erb KH, Krausmann F (2014) Human Appropriation of Net Primary Production: Patterns, Trends, and Planetary Boundaries. Annu Rev Environ Resour 39: 363-91

Haberl H, Erb KH, Krausmann F, Gaube V, Bondeau A, Plutzar C, Gingrich S, Lucht W, Fischer-Kowalski M (2007) Quantifying and mapping the human appropriation of net primary production in earth's terrestrial ecosystems. PNAS 104: 12942-5

Haberl H, Erb KH, Krausmann F, Loibl W, Schulz N, Weisz H (2001) Changes in ecosystem processes induced by land use: Human appropriation of aboveground NPP and its influence on standing crop in Austria. Global Biogeochem Cycles 15: 929-42

Haberl H, Schulz NB, Plutzar C, Erb KH, Krausmann F, Loibl W, Moser D, Sauberer N, Weisz H, Zechmeister HG, Zulka P (2004) Human appropriation of net primary production and species diversity in agricultural landscapes. Agric Ecosyst Environ 102: 213-8

Hua X (2009) Quantifying the Human Appropriation of Net Primary Production and analysis of its multi-year changes in Guangdong. Sun Yat-sen University.
Huang Q, Zhang FY, Zhang Q, Ou H, Jin YX (2020) Quantitative Assessment of the Impact of Human Activities on Terrestrial Net Primary Productivity in the Yangtze River Delta. Sustainability 12: 16
Huang X, Luo G, Han Q (2018) Temporospatial patterns of human appropriation of net primary production in Central Asia grasslands. Ecol. Indic. 91: 555-61
Huang Y, Zhang W, Sun W, Zheng X (2007) NET PRIMARY PRODUCTION OF CHINESE CROPLANDS FROM 1950 TO 1999. Ecological Applications 17: 692-701
Kastner T (2009) Trajectories in human domination of ecosystems: Human appropriation of net primary production in the Philippines during the 20th century. Ecological Economics 69: 260-9
Knauer, K., U. Gessner, R. Fensholt and C. Kuenzer. 2016. An ESTARFM Fusion Framework for the Generation of Large-Scale Time Series in Cloud-Prone and Heterogeneous Landscapes. Remote Sensing 8(5): 425.
Kohlheb N, Krausmann F (2009) Land use change, biomass production and HANPP: The case of Hungary 1961-2005. Ecological Economics 69: 292-300
Krausmann F, Erb K-H, Gingrich S, Haberl H (2013) Global human appropriation of net primary production doubled in the 20th century. PNAS 110: 10324–9
Krausmann F, Gingrich S, Haberl H, Erb KH, Musel A, Kastner T, Kohlheb N, Niedertscheider M, Schwarzlmuller E (2012) Long-term trajectories of the human appropriation of net primary production: Lessons from six national case studies. Ecological Economics 77: 129-38
Li F, Meng J (2018) Temporal and Spatial Variation of Human Appropriation of Net Primary Productivity in the Middle Reaches of the Heihe River Basin. ARID ZONE RESEARCH 35: 743-52
Liao CH, Wang JF, Dong TF, Shang JL, Liu JG, Song Y (2019) Using spatio-temporal fusion of Landsat-8 and MODIS data to derive phenology, biomass and yield estimates for corn and soybean. Sci. Total Environ. 650: 1707-21
Lieth H. 1975. Modeling the Primary Productivity of the World: Springer Berlin Heidelberg.
M. VP, R. EP, H. EA, A. MP (1986) Human Appropriation of the Products of Photosynthesis. BioScience 6: 6
Mann HB (1945) NONPARAMETRIC TESTS AGAINST TREND. Econometrica 13: 245-59
Musel A (2009) Human appropriation of net primary production in the United Kingdom, 1800-2000 Changes in society's impact on ecological energy flows during the agrarian-industrial transition. Ecological Economics 69: 270-81
Nduati E, Sofue Y, Matniyaz A, Park JG, Yang W, Kondoh A (2019) Cropland Mapping Using Fusion of Multi-Sensor Data in a Complex Urban/Peri-Urban Area. Remote Sensing 11: 24
Niedertscheider M, Erb K (2014) Land system change in Italy from 1884 to 2007: Analysing the North–South divergence on the basis of an integrated indicator framework. Land Use Policy 39: 366-75
Niedertscheider M, Gingrich S, Erb KH (2012) Changes in land use in South Africa between 1961 and 2006: an integrated socio-ecological analysis based on the human appropriation of net primary production framework. Regional Environmental Change 12: 715-27
Niedertscheider M, Kuemmerle T, Muller D, Erb KH (2014) Exploring the effects of drastic institutional and socio-economic changes on land system dynamics in Germany between 1883 and 2007. Global Environmental Change-Human and Policy Dimensions 28: 98-108
Niedertscheider M, Tasser E, Patek M, Rudisser J, Tappeiner U, Erb KH (2017) Influence of Land-Use Intensification on Vegetation C-Stocks in an Alpine Valley from 1865 to 2003. Ecosystems 20:

1391-406
O'Neill DW, Tyedmers PH, Beazley KF (2007) Human appropriation of net primary production (HANPP) in Nova Scotia, Canada. Regional Environmental Change 7: 1-14
Pachavo G, Murwira A (2014) Remote sensing net primary productivity (NPP) estimation with the aid of GIS modelled shortwave radiation (SWR) in a Southern African Savanna. Int J Appl Earth Obs Geoinf 30: 217-26
Plutzar C, Kroisleitner C, Haberl H, Fetzel T, Bulgheroni C, Beringer T, Hostert P, Kastner T, Kuemmerle T, Lauk C, Levers C, Lindner M, Moser D, Muller D, Niedertscheider M, Paracchini M, Schaphoff S, Verburg PH, Verkerk PJ, Erb KH (2016) Changes in the spatial patterns of human appropriation of net primary production (HANPP) in Europe 1990-2006. Regional Environmental Change 16: 1225-38
Roy DP, Kovalskyy V, Zhang HK, Vermote EF, Yan L, Kumar SS, Egorov A (2016) Characterization of Landsat-7 to Landsat-8 reflective wavelength and normalized difference vegetation index continuity. Remote Sens Environ 185: 57-70
Running SW (2012) A Measurable Planetary Boundary for the Biosphere. Science 337: 1458-9
Schmidt M, Lucas R, Bunting P, Verbesselt J, Armston J (2015) Multi-resolution time series imagery for forest disturbance and regrowth monitoring in Queensland, Australia. Remote Sens Environ 158: 156-68
Schwarzlmuller E (2009) Human appropriation of aboveground net primary production in Spain, 1955-2003: An empirical analysis of the industrialization of land use. Ecological Economics 69: 282-91
Sen, Kumar P (1968) Estimates of the Regression Coefficient Based on Kendall\"s Tau. Publications of the American Statistical Association 63: 1379-89
Song CQ, Ke LH, Pan H, Zhan SN, Li K, Ma RH (2018) Long-term surface water changes and driving cause in Xiong'an, China: from dense Landsat time series images and synthetic analysis. Science Bulletin 63: 708-16
Tang J, Zeng J, Zhang L, Zhang R, Li J, Li X, Zou J, Zeng Y, Xu Z, Wang Q, Zhang Q (2020a) A modified flexible spatiotemporal data fusion model. Front Earth Sci doi: 10.1007/s11707-019-0800-x
Tang J, Zeng J, Zhang Q, Zhang R, Leng S, Zeng Y, Shui W, Xu Z, Wang Q (2020b) Self-adapting extraction of cropland phenological transitions of rotation agroecosystems using dynamically fused NDVI images. Int J Biometeorol 4: 1-11
Wang HB, Li X, Ma MG, Geng LY (2019) Improving Estimation of Gross Primary Production in Dryland Ecosystems by a Model-Data Fusion Approach. Remote Sensing 11: 22
Wang PJ, Wu DR, Yang JY, Ma YP, Feng R, Huo ZG (2020) Summer maize growth under different precipitation years in the Huang-Huai-Hai Plain of China. Agric For Meteorol 285: 12
Wang Q, Wu J, Li X, Zhou H, Yang J, Geng G, An X, Liu L, Tang Z (2017a) A comprehensively quantitative method of evaluating the impact of drought on crop yield using daily multi-scale SPEI and crop growth process model. Int J Biometeorol 61: 685-99
Wang QF, Zeng JY, Leng S, Fan BX, Tang J, Jiang C, Huang Y, Zhang Q, Qu YP, Wang WL, Shui W (2018) The effects of air temperature and precipitation on the net primary productivity in China during the early 21st century. Front Earth Sci 12: 818-33
Wang SS, Mo XG, Liu ZJ, Baig MHA, Chi WF (2017b) Understanding long-term (1982-2013) patterns and trends in winter wheat spring green-up date over the North China Plain. Int J Appl Earth Obs Geoinf 57: 235-44
Wang XY, Xue S, Xie GH (2012) Value-taking for residue factor as a parameter to assess the field residue

661 of field crops. Journal of China Agricultural University
662 Warman RD (2014) Global wood production from natural forests has peaked. Biodivers. Conserv. 23:
663 1063-78
664 Xie G, Han D, Wang X, Lu R (2011) Harvest index and residue factor of cereal crops in China. Journal
665 of China Agricultural University 16: 1-8
666 Xie SL, Su YB, Xu WH, Cai WB, Wang XK, Lu F, Ouyang ZY (2019) The effect of habitat changes
667 along the urbanization gradient for breeding birds: an example from the Xiong'an New Area. Peerj
668 7: 22
669 Xu CL, Tao HB, Tian BJ, Gao YB, Ren JH, Wang P (2016) Limited-irrigation improves water use
670 efficiency and soil reservoir capacity through regulating root and canopy growth of winter wheat.
671 Field Crops Res. 196: 268-75
672 Xu F, Yang ZF, Chen B, Zhao YW (2013) Impact of submerged plants on ecosystem health of the plant-
673 dominated Baiyangdian Lake, China. Ecol Modell 252: 167-75
674 Xu HQ, Shi TT, Wang MY, Fang CY, Lin ZL (2018) Predicting effect of forthcoming population growth-
675 induced impervious surface increase on regional thermal environment: Xiong'an New Area, North
676 China. Build Environ 136: 98-106
677 Xu ZX, Chen YN, Li JY (2004) Impact of climate change on water resources in the Tarim River basin.
678 Water Resour. Manag. 18: 439-58
679 Zhang FY, Pu LJ, Huang Q (2015) Quantitative Assessment of the Human Appropriation of Net Primary
680 Production (HANPP) in the Coastal Areas of Jiangsu, China. Sustainability 7: 15857-70
681 Zhang Y, Pan Y, Zhang X, Wu J, Yu C, Li M, Wu J (2018) Patterns and dynamics of the human
682 appropriation of net primary production and its components in Tibet. J. Environ. Manage. 210: 280-
683 9
684 Zhao N, Yue TX, Li H, Zhang LL, Yin XZ, Liu Y (2018) Spatio-temporal changes in precipitation over
685 Beijing-Tianjin-Hebei region, China. Atmos Res 202: 156-68
686 Zhou C, Elshkaki A, Graedel TE (2018) Global Human Appropriation of Net Primary Production and
687 Associated Resource Decoupling: 2010-2050. Environ. Sci. Technol. 52: 1208-15
688 Zhou Q, Zhao X, Wu DH, Tang RY, Du XZ, Wang HY, Zhao JC, Xu PP, Peng YF (2019) Impact of
689 Urbanization and Climate on Vegetation Coverage in the Beijing-Tianjin-Hebei Region of China.
690 Remote Sensing 11: 16
691 Zhu W, Pan Y, Zhang J (2007) ESTIMATION OF NET PRIMARY PRODUCTIVITY OF CHINESE
692 TERRESTRIAL VEGETATION BASED ON REMOTE SENSING. J Plant Ecol 31: 413-24
693 Zhu X, Chen J, Gao F, Chen X, Masek JG (2010) An enhanced spatial and temporal adaptive reflectance
694 fusion model for complex heterogeneous regions. Remote Sens Environ 114: 2610-23
695 Zhu X, Helmer EH, Gao F, Liu D, Chen J, Lefsky MA (2016) A flexible spatiotemporal method for fusing
696 satellite images with different resolutions. Remote Sens Environ 172: 165-77
697
698

Figures

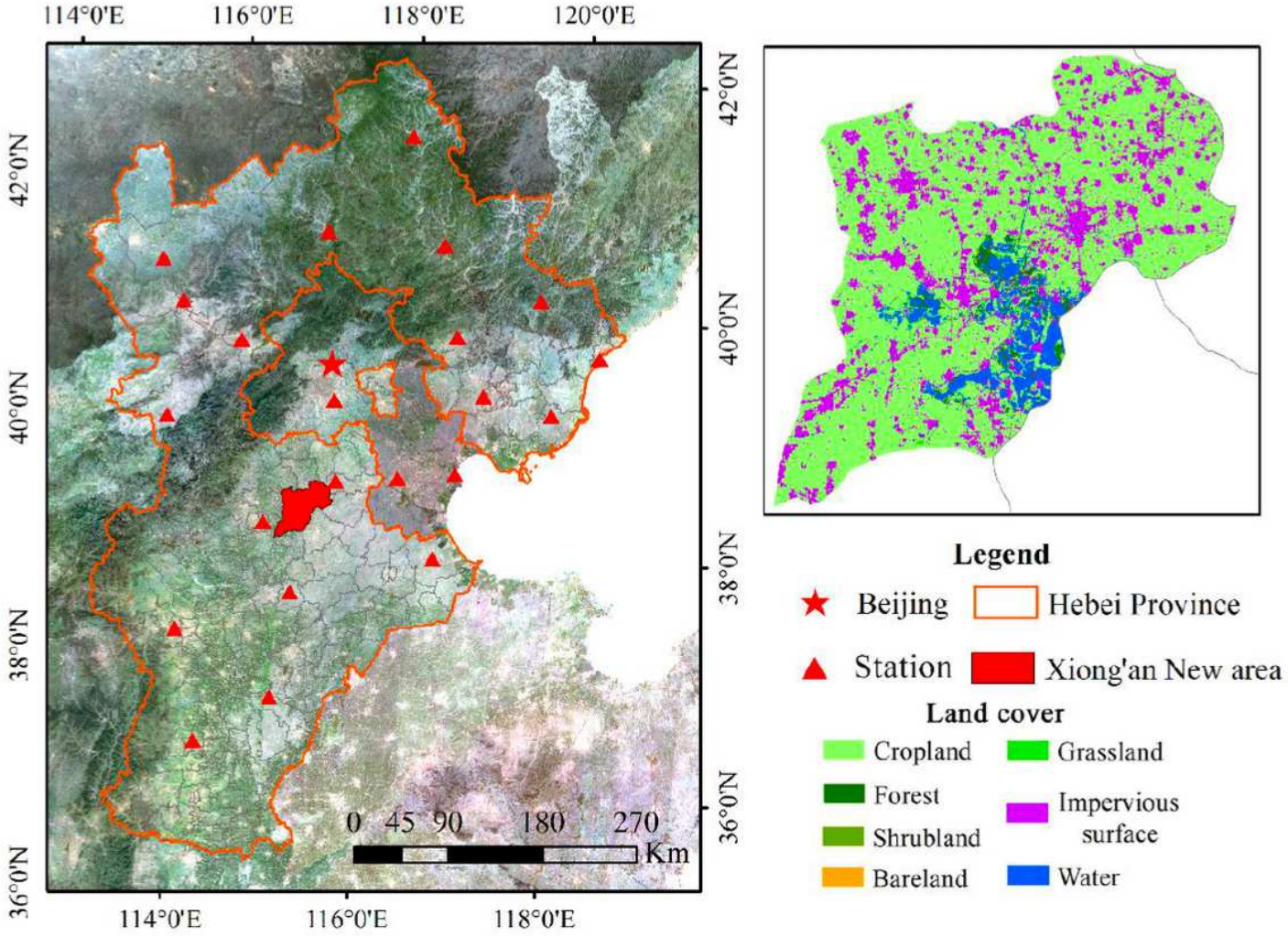

Figure 1

Location and land cover map of Xiong'an New Area. Note: The designations employed and the presentation of the material on this map do not imply the expression of any opinion whatsoever on the part of Research Square concerning the legal status of any country, territory, city or area or of its authorities, or concerning the delimitation of its frontiers or boundaries. This map has been provided by the authors.

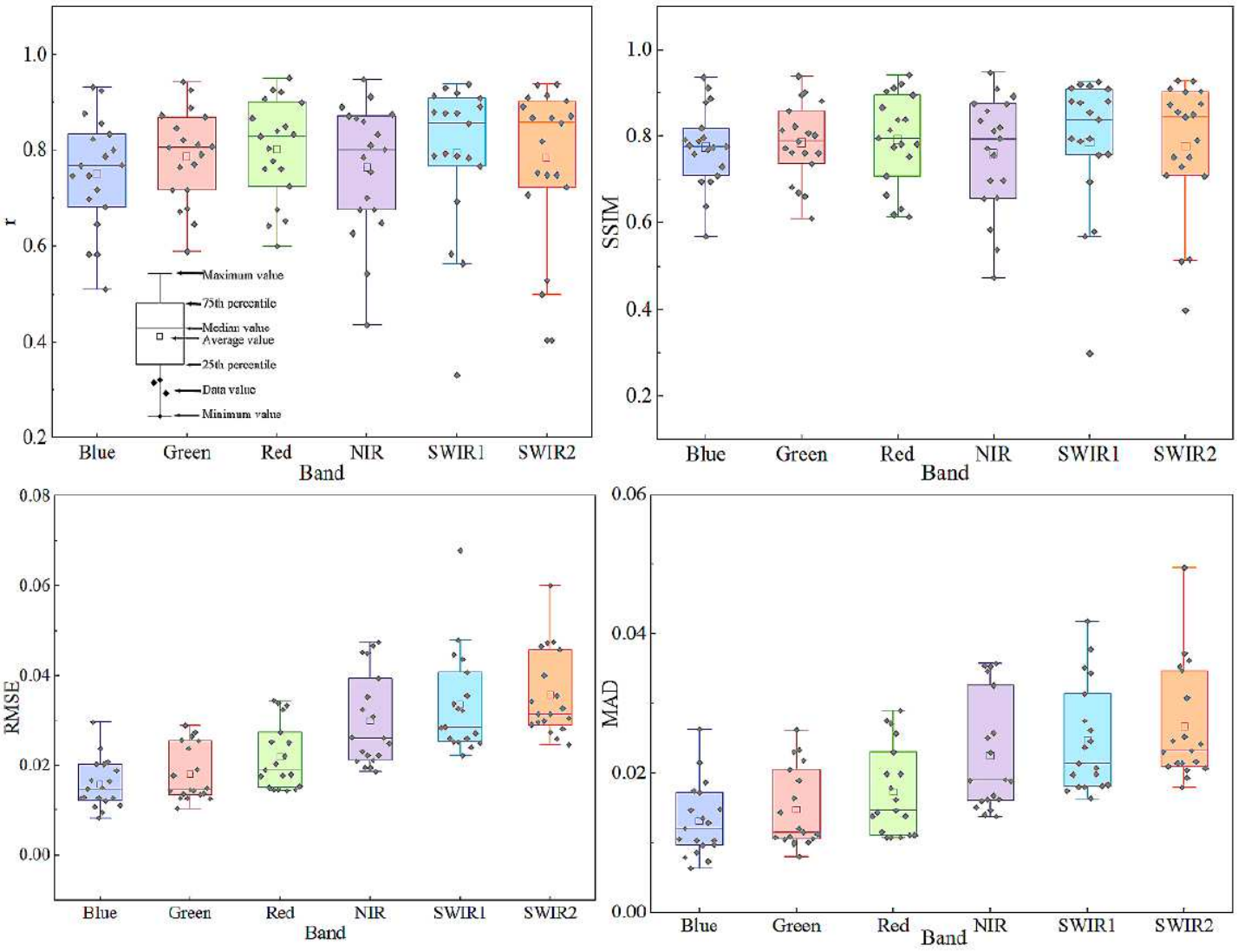

Figure 2

Accuracy of multiple indicators for the fusion images from 2000 to 2018: (a) r, (b) SSIM, (c) RMSE, and (d) MAD

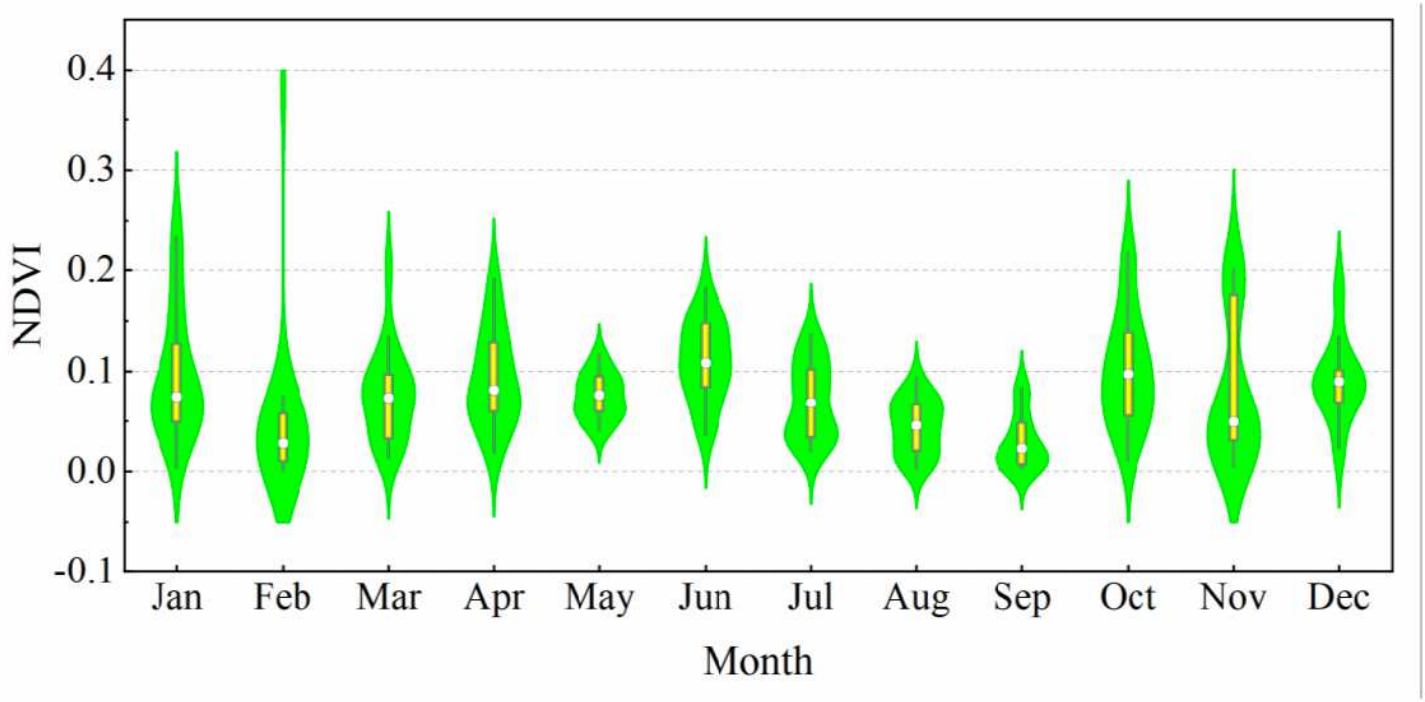

Figure 3

ΔΔNDVI distribution of each month from 2000 to 2018

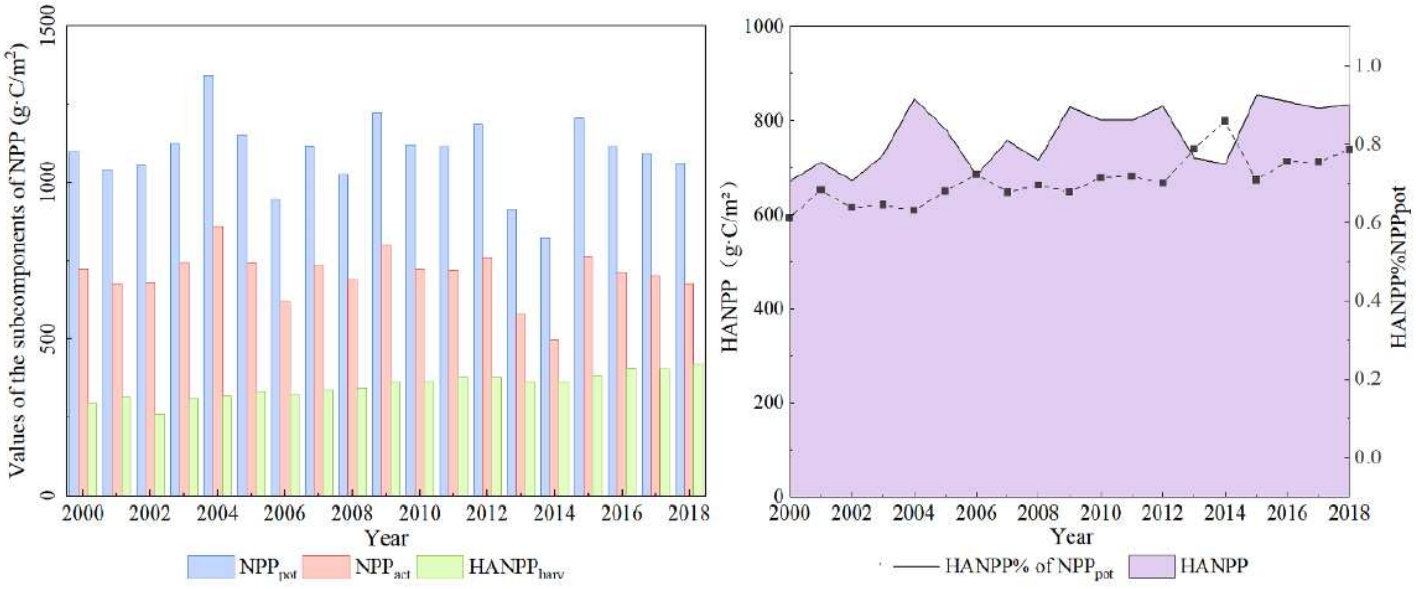

Figure 4

Change of the HANPP and its subcomponents and the ratio to NPPpot: (a) subcomponents and (b) HANPP

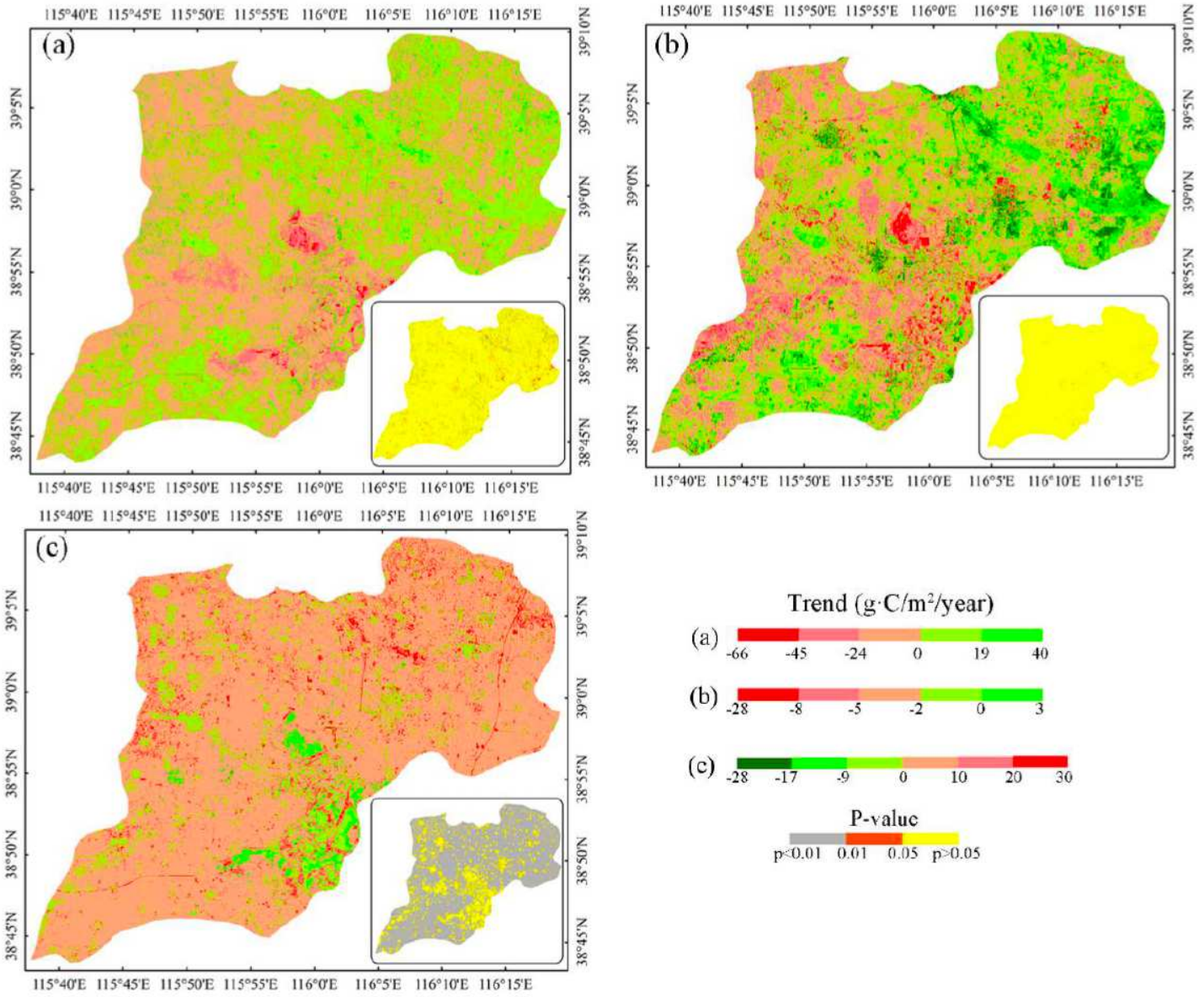

Figure 5

Spatial trend and corresponding significant level of the HANPP subcomponents: (a) NPPpot; (b) NPPact; and (c): HANPPharv. Note: The designations employed and the presentation of the material on this map do not imply the expression of any opinion whatsoever on the part of Research Square concerning the legal status of any country, territory, city or area or of its authorities, or concerning the delimitation of its frontiers or boundaries. This map has been provided by the authors.

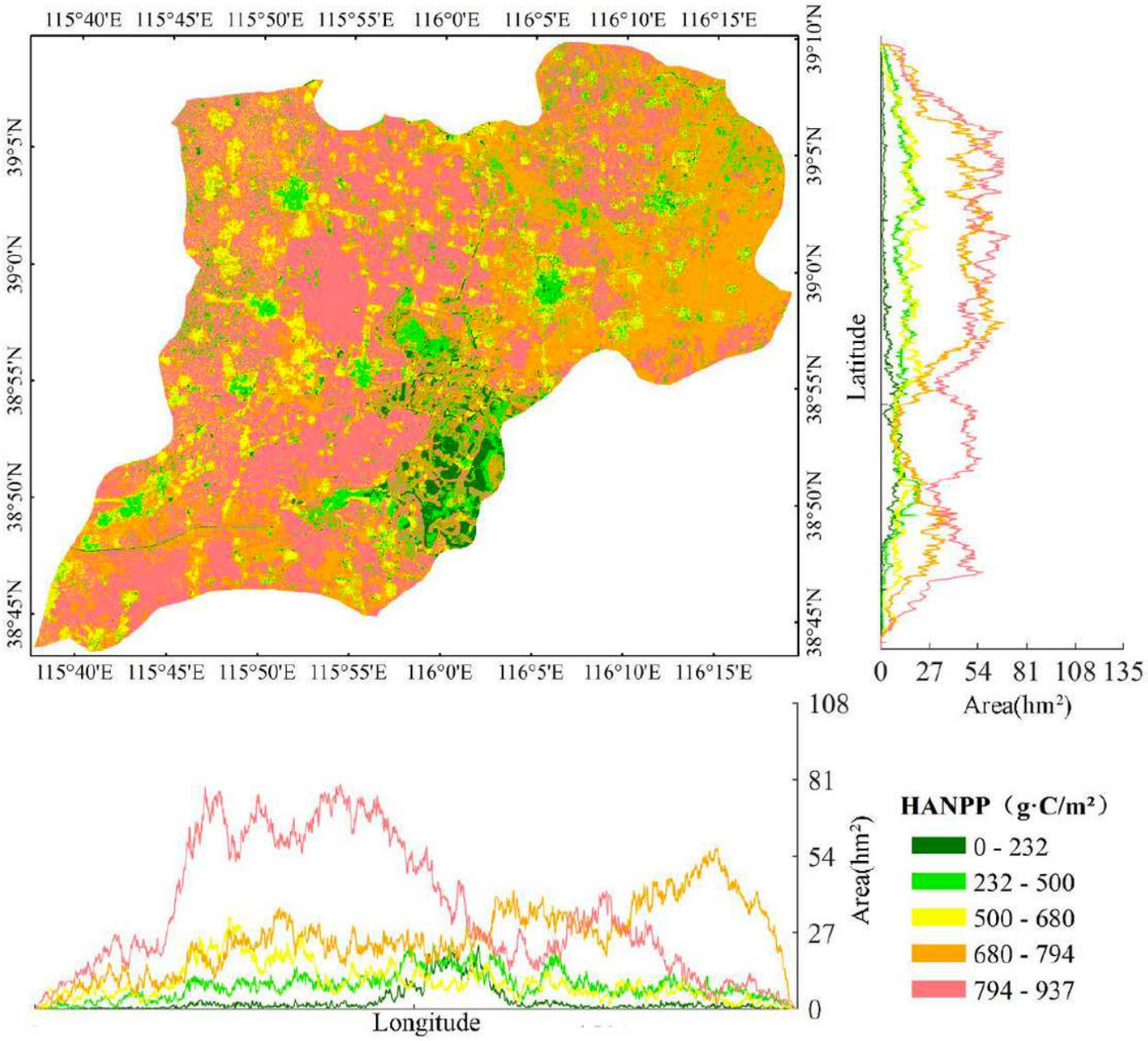

Figure 6

Spatial pattern of the HANPP in Xiong'an New Area. Note: The designations employed and the presentation of the material on this map do not imply the expression of any opinion whatsoever on the part of Research Square concerning the legal status of any country, territory, city or area or of its authorities, or concerning the delimitation of its frontiers or boundaries. This map has been provided by the authors.

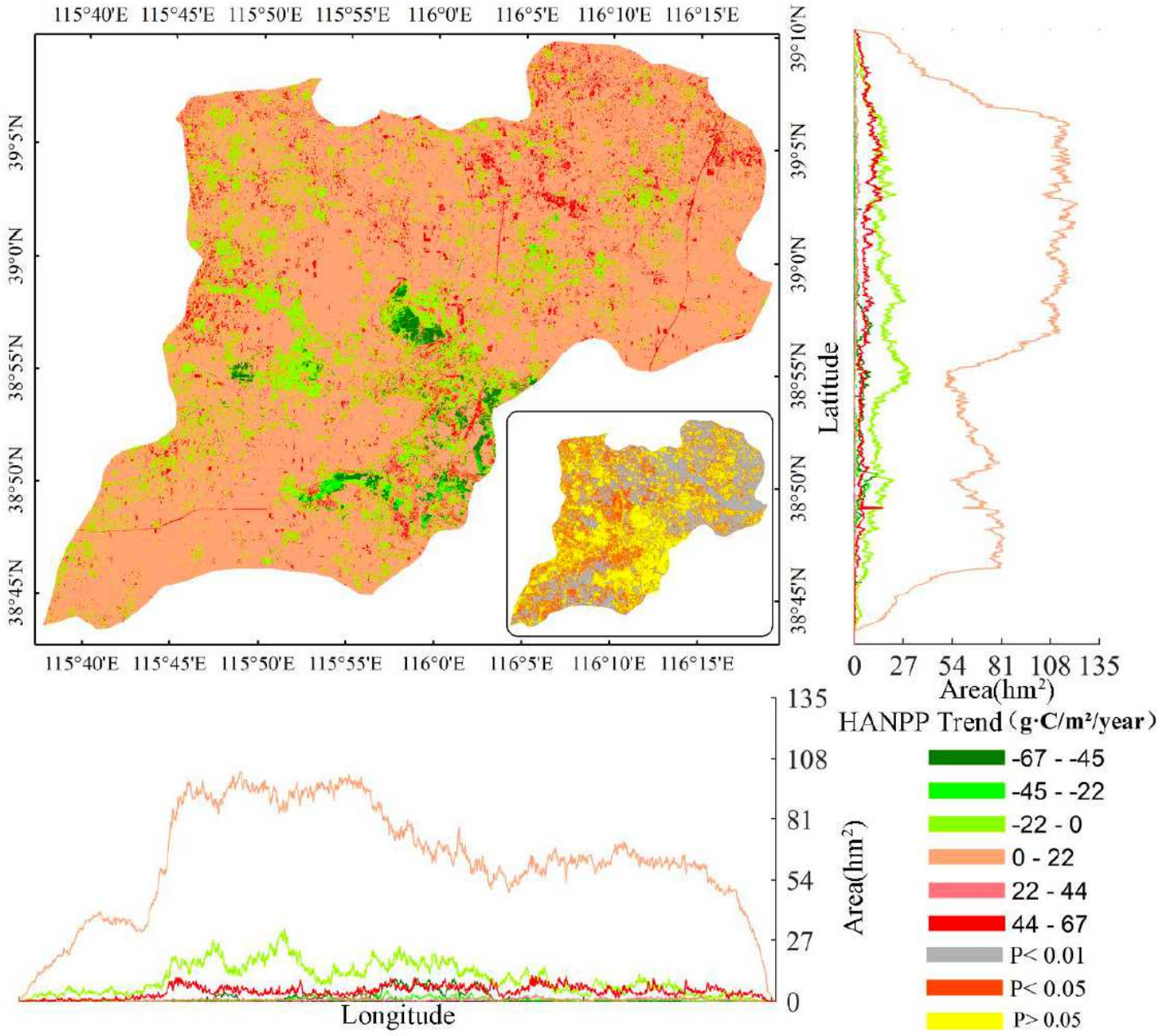

Figure 7

Spatial trend of the HANPP in Xiong'an New Area. Note: The designations employed and the presentation of the material on this map do not imply the expression of any opinion whatsoever on the part of Research Square concerning the legal status of any country, territory, city or area or of its authorities, or concerning the delimitation of its frontiers or boundaries. This map has been provided by the authors.

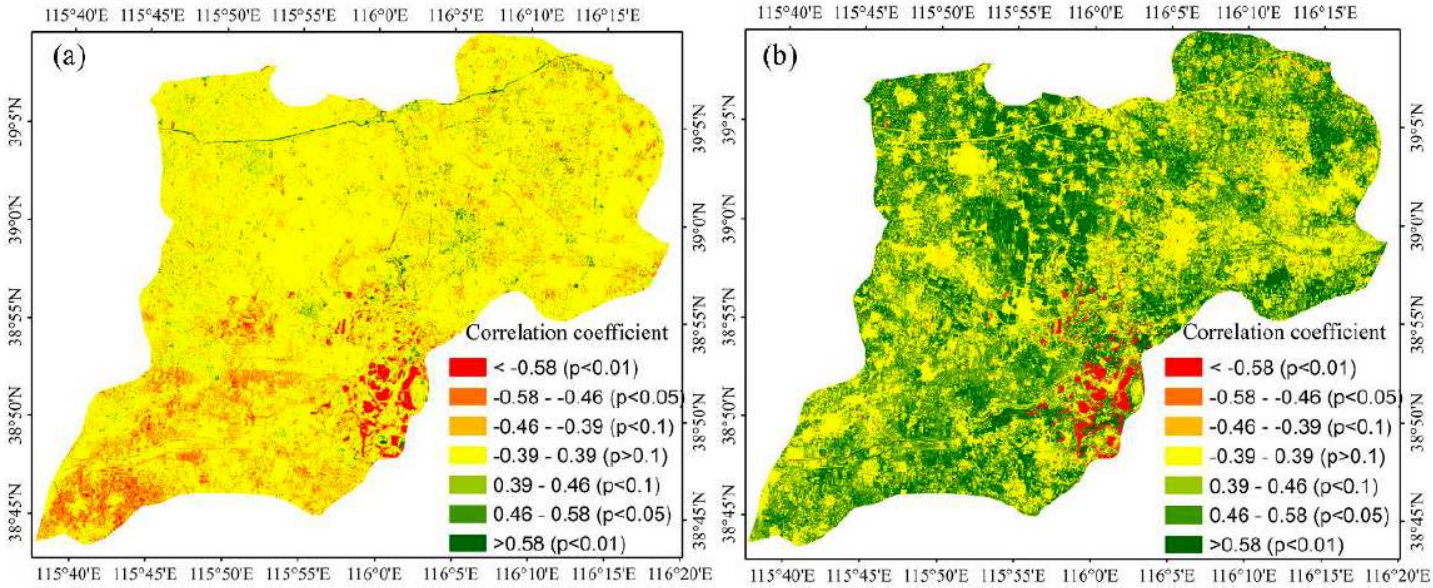

Figure 8

Correlation between climate factors and the HANPP in Xiong'an New Area: (a) temperature and (b) precipitation. Note: The designations employed and the presentation of the material on this map do not imply the expression of any opinion whatsoever on the part of Research Square concerning the legal status of any country, territory, city or area or of its authorities, or concerning the delimitation of its frontiers or boundaries. This map has been provided by the authors.

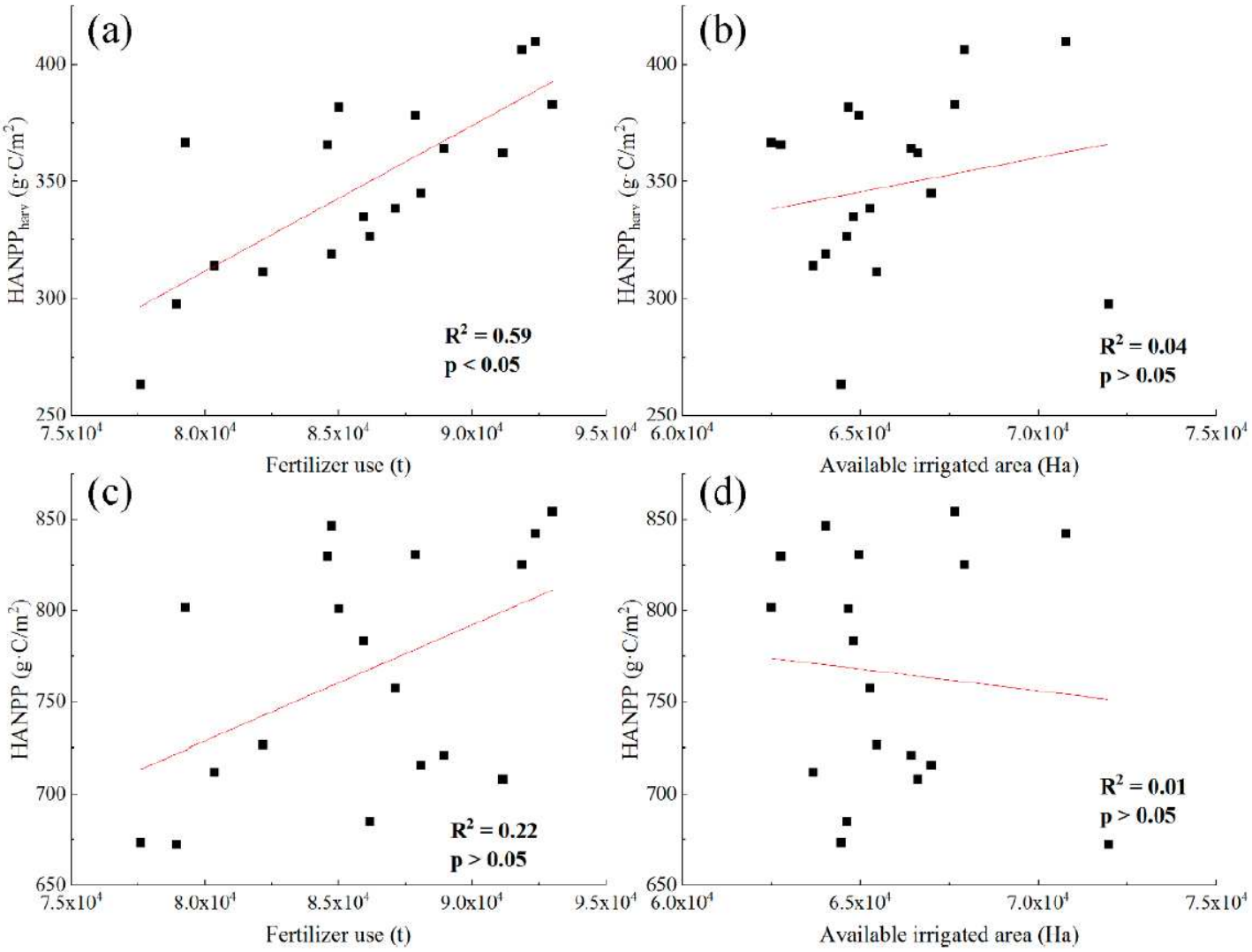

Figure 9

Correlation of agricultural conditions with the HANPP elements: (a) fertilizer use and HANPPharv; (b) available irrigated area and HANPPharv; (c) fertilizer use and HANPP; and (d) available irrigated area and HANPP

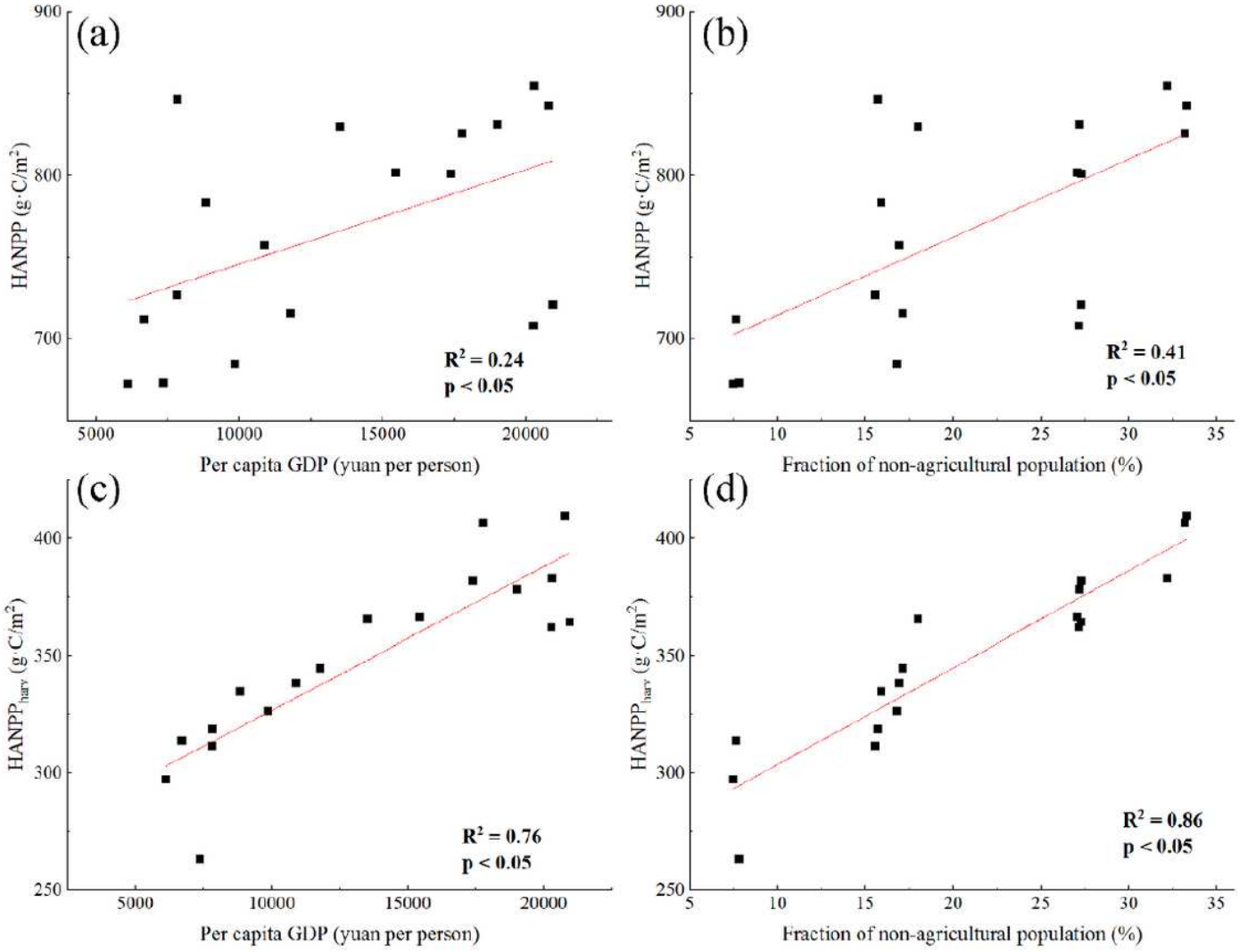

Figure 10

Correlation between the socio-economic conditions and the HANPP elements: (a) per capita GDP and HANPP; (b) fraction of the non-agricultural population and the HANPP; (c) per capita GDP and HANPPharv; and (d) fraction of the non-agricultural population and HANPPharv